A multi-decadal view of the heat and mass budget of a volcano in unrest: La Soufrière de Guadeloupe (French West Indies)

David E Jessop, Séverine Moune, Roberto × Moretti, Dominique Gibert, Jean-Christophe Komorowski, Vincent Robert, Michael J. Heap, Alexis Bosson, Magali Bonifacie, Sébastien Deroussi, et al.

Bulletin of Volcanology manuscript No.
(will be inserted by the editor)

A multi-decadal view of the heat and mass budget of a volcano in unrest: La Soufrière de Guadeloupe (French West Indies)

David E. Jessop · Séverine Moune · Roberto Moretti · Dominique Gibert · Jean-Christophe Komorowski Vincent Robert · Michael J. Heap · Alexis Bosson · Magali Bonifacie · Sébastien Deroussi · Céline Dessert · Marina Rosas-Carbajal · Arnaud Lemarchand · Arnaud Burtin

Received: date / Accepted: date

Orcid IDs:
David E. Jessop: 0000-0003-2382-219X
Severine Moune: 0000-0002-8485-0154
Roberto Moretti: 0000-0003-2031-5192
Jean-Christophe Komorowski: 0000-0002-6874-786X
Vincent Robert: 0000-0002-9016-7167
Michael J. Heap: 0000-0002-4748-735X
Marina Rosas-Carbajal: 0000-0002-5393-0389

Abstract Particularly in the presence of a hydrothermal system, volcanoes output great amounts of heat primarily through the transport of water from deep within the edifice to the surface. Thus, heat flux is a prime tool for evaluating volcanic activity and unrest. We review the volcanic unrest at La Soufrière de Guadeloupe (French West Indies) using an airborne thermal camera survey, and in-situ measurements (temperature and flow rate). We deduce mass and heat fluxes for the fumarolic, ground and thermal spring outputs and follow these over a period spanning 20 years. We compare our results to published data to and perform a retrospective analysis of the temporal variations in heat flux over this period.

We find that the heat emitted by the volcano is 36.5 ± 7.9 MW, of which the fumarolic heat flux is dominant at 28.3 ± 6.8 MW. Given a total heated area of $26\,279\,\mathrm{m}^2$, this equates to a heat-flux

D. E. Jessop
Tel.: (+590) 590 99-1137
E-mail: d.jessop@opgc.fr

density of $627 \pm 94\,\mathrm{W/m^2}$, which value is amongst the highest established for worldwide volcanoes with hydrothermal systems, particularly for dome volcanoes. A major change at La Soufrière de Guadeloupe, however, is the development of a widespread region of ground heating at the summit where heat output has increased from $0.2 \pm 0.1\,\mathrm{MW}$ in 2010 to $5.7 \pm 0.9\,\mathrm{MW}$ in the present study. This change is concurrent with accelerating unrest at the volcano, and the emergence of new high-flux fumaroles in recent years. Our findings highlight the need for continued and enhanced surveillance and research strategies at La Soufrière de Guadeloupe, the results of which can be used to better understand hydrothermal volcanism the world over.

Keywords Heat and mass flux · airborne thermal imagery · Pitot tube · MultiGAS · fumarole

1 Introduction

Hydrothermal-volcanic systems in active island-arc andesite volcanoes are produced by the interaction of hot magmatic fluids with the marine or meteoric water at shallower depths and the host-rock (e.g. Sigurdsson et al., 2015; Hedenquist and Lowenstern, 1994). Such volcanoes can undergo sudden and catastrophic changes in behaviour and two events in recent years have particularly highlighted the importance of understanding all aspects of hydrothermal volcanoes and their hazardous behaviour: the September 2014 Ontake (Japan) and December 2019 Whakaari (White Island, New Zealand) eruptions, both of which resulted in the tragic loss of human life.

Cooling through interaction with water (absorption into deep groundwaters and mixing with meteoric and sea-water) and the host-rock at hydrothermal volcanic systems strongly modifies the geochemical profile of deep fluids produced by magma degassing (essentially water, CO_2, H_2S and/or SO_2 and HCl, e.g. Giggenbach, 1975; Moretti and Stefansson, 2020). The boiling of the formed geothermal liquids liberates dissolved gases, which fractionate into the vapour phase that ascends to the surface through steam-dominated fumaroles. Condensation of these vapours into groundwaters may generate steam-heated waters likely to flow out laterally where they can further mix with external waters and discharge as thermal springs (Hedenquist and Lowenstern, 1994; Sigurdsson et al., 2015). Therefore, significant amounts of heat are emitted as the superheated steam generated by these interactions rises towards the surface through networks of cracks, fissures and more porous rock within the edifice. The superheated steam either locally condensates near the surface or escapes to the atmosphere through fumaroles (Chiodini et al., 2001; Fischer and Chiodini, 2015; Stimac et al., 2015). Heat emissions can occur in several forms. First, where resistance to flow is low (high permeability subsurface) and the steam reaches the surface without condensing and, second, where resistance to flow is high (low permeability subsurface) and the steam condenses near the surface. In this scenario, the fumarolic output is high and significant amounts of heat and mass

are transferred to the environment. Second, fumarolic output is correspondingly lower and heat is brought to the surface by conduction and liberated to the environment by radiation and forced convection (Harris, 2013; Gaudin et al., 2016). This latter scenario leads to thermal anomalies (ground heating) and small, very low-flux fumaroles typically distributed over quite large areas (cf. Aubert et al., 1984; Aubert, 1999; Harris and Stevenson, 1997; Harris and Maciejewski, 2000, for example). In many cases, this far exceeds the fumarolic output in terms of energy transfer (e.g. Matsushima et al., 2003; Mannini et al., 2019). Due to the high heat capacity of water, direct fumarolic degassing and diffuse small fumarole/soil degassing are generally the two major components of heat loss at hydrothermal volcanic systems (Aubert, 1999; Chiodini et al., 2001). The final component of heat transfer in hydrothermal volcanic systems is through a network of thermal springs which typically appear along the flanks or base of the system, taking advantage of structural discontinuities. These springs discharge water, initially heated by volcanic gases, that has either condensed deep within the edifice or nearer the surface when it has come into contact with the water table (Fischer and Chiodini, 2015; Stimac et al., 2015).

Whilst the degree and importance of the aforementioned components will vary from volcano to volcano and may vary in time at a given site, volcanic heat flow in general is indicative of (e.g. Hardee, 1982; Lardy and Tabbagh, 1999; Harris et al., 2009): 1. The state and position of the magma body. 2. The porosity/permeability of the edifice or dome. 3. The extent of infiltration of external water into the system. As such its spatio-temporal variations are of particular importance for both monitoring and fundamental research, because understanding and modelling of such variations considerably narrows the domain of solutions due to the points raised above to a set that are very similar (temporal similarity) and congruent (spatially similar) (Di Renzo et al., 2016).

The hydrothermal system plays a fundamental role in providing and enhancing the physico-chemical conditions that promote rock alteration, as well as the pressurisation of hydrothermal fluids. These processes act as strong forcing and triggering agents on the dynamics of volcanic activity by promoting the mechanical weakening of edifice-forming volcanic rock (Pola et al., 2012; Wyering et al., 2014; Heap et al., 2015; Mordensky et al., 2019) and therefore recurrent partial flank collapses (López and Williams, 1993; de Vries et al., 2000; Reid et al., 2001; Reid, 2004; John et al., 2008), as observed at La Soufrière de Guadeloupe (Komorowski et al., 2005; Rosas-Carbajal et al., 2016). Escalating pressurisation of hydrothermal systems as a result of permeability loss due to hydrothermal alteration can also lead to explosive activity (e.g. Heap et al., 2019) that can reach paroxysmal levels with non-magmatic laterally-directed turbulent pyroclastic density currents or blasts (e.g. Bandaisan, Japan, in 1889). Hydrothermal alteration has also been observed to reduce the thermal conductivity and thermal diffusivity of andesite for a given porosity (Heap et al., 2020). Finally, the hydrothermal system is a strong modulator of geophysical and geochemical

signals of magmatic unrest and can generate a plethora of unrest non-magmatic signals that render monitoring, as well the interpretation of the complexity of coupled processes and forecasting of their evolution towards eruptive unrest, very challenging.

In this paper, we concentrate on the use of thermal measurements to infer the state of unrest of a major hydrothermal volcanic system, that of La Soufrière de Guadeloupe (Lesser Antilles). La Soufrière de Guadeloupe is an ideal target for such a study due to the wealth of geochemical, geological and geophysical data acquired on the volcano. As such it is often considered a natural laboratory for andesitic hydrothermal volcanoes.

2 Context

La Soufrière de Guadeloupe (16.0446° N, −61.6642° E, alt. 1467 m) is an andesitic dome volcano situated in the south of the Basse-Terre island of Guadeloupe (French West Indies), which is part of the Lesser Antilles volcanic arc and is the most recent edifice of the Grande Découverte complex (445 ka). La Soufrière de Guadeloupe is amongst the most active and potentially deadly of the volcanoes in the Lesser Antilles Arc (Komorowski et al., 2005). Hydrothermal activity is sustained by gas and heat transfer from a 6–7 km deep andesitic magma reservoir to shallower aquifers (Pichavant et al., 2018). Owing to an extensive hydrothermal system, La Soufrière de Guadeloupe has undergone a series of six phreatic and hydrothermal explosive eruptions (Komorowski et al., 2005) since the last major magmatic eruption in 1530 C.E.. The last, and probably most famous, eruption was in 1976–77 (e.g. Feuillard et al., 1983; Hincks et al., 2014).

The present edifice dates back to at least 9150 years (Komorowski et al., 2005; Legendre, 2012), during which time several major magmatic eruptions have occurred, the latter in around 1530 C.E. at which time the current dome was emplaced (Komorowski et al., 2005; Boudon et al., 2008). Since this last magmatic event, there has been a number of phreatic and/or hydrothermal explosive eruptions. The last eruption occurred in 1976–77, following which the volcano became essentially dormant until 1992 when seismic activity and steam emissions from summit fumaroles recommenced (OVSG-IPGP 1999-2001[1]; Zlotnicki et al., 1992; Komorowski et al., 2001, 2005). Summit degassing has gradually increased concomitantly with other observables (seismic, gas flux and concentration, ground and fumarole temperatures, deformation, emissions of chlorine-rich acid gases) over the past 30 years including the apparition of two new high-flux fumaroles (Napoléon Nord and Napoléon Est, labeled NAPN and NPE on Fig. 1; OVSG-IPGP 2014-2016; Komorowski et al., 2005; Villemant et al., 2014; Moretti et al., 2020a), extensive zones of substantial surface heating and "scalding" of the vegetation. Several fumarolic sites on the flanks characterised by a low state of activity since 1976 gradually vanished, with Tarissan (TAS), Cratère Sud (CS), la Fente

[1] http://www.ipgp.fr/fr/ovsg/bulletins-mensuels-de-lovsg

du Nord, Gouffre 56 (G56) and the Lacroix fumerolles all becoming inactive by 1984 (Komorowski et al., 2005; Boichu et al., 2011; Ruzié et al., 2013, Feuillard, 2011[2]).

A spike in activity in 2018 increased speculation that the volcano is in a state of growing unrest and is likely to undergo another eruptive episode in the near future (Moretti et al., 2020a). This uncertainty as to the ongoing evolution of the volcano is further evidenced by the fact that, until 2014, ground thermal anomalies and accompanying soil degassing had likely been limited to the areas directly surrounding the major fumaroles, as well as the Faille de la Ty/Ravine Claire/Matylis structure (Fig. 1; OVSG-IPGP 2014-2020; Komorowski et al., 2005; Lesparre et al., 2012; Brothelande et al., 2014). In recent years, however, a number of thermal anomalies and altered zones have been observed such as at the Zone Fumerolienne Napoléon Nord (ZFNN) at the summit, delimited by NAPN, Cratère Dupuy (DUP) and TAS, adjoining the Breislack fault (BLK) and in the upper Matylis ravine (Fig. 1, OVSG-IPGP 2014-2020 and this work). Relatedly, increasing fluxes and acidification of the water and gas rising up within the volcano has led to significant alteration and weakening of the edifice, leaving it vulnerable to flank collapse during even moderate seismic activity or extreme rainfall (Komorowski et al., 2005; Rosas-Carbajal et al., 2016).

The summit vents are located near major fractures and fault zones, i.e. zones of high vertical permeability (Zlotnicki et al., 1992; Komorowski et al., 2005). These are likely to have acted as a route of ascent for the magma that formed the dome (Brombach et al., 2000), the deepest part of which acts as a zone of preferential input of magmatic gases into the hydrothermal aquifer, and its shallowest part behaves as a zone of preferential discharge for the hydrothermal aquifer (Brombach et al., 2000). The horse-shoe shaped scar of recurrent partial edifice collapses of at least the last 3000 years, including the major Amic Crater (1370 BCE) and the 1530 CE events, form a listric clay-rich low-permeability south-sloping surface for preferential outflow of groundwaters that were heated. This led to the emergence of a number of thermal springs (Brombach et al., 2000; Villemant et al., 2005; Ruzié et al., 2013; Villemant et al., 2014). Here, fluids are heated within the hydrothermal system and then cooled to some degree by mixing with meteoric water before escaping to the environment.

3 Materials and methods

Here we present the first study that fully integrates measurements of all the heat sources that span over the same time window (typically monthly, from 2000-present day). Therefore, they are contemporaneous even if sampling rates are different between different methods and sites.

[2] Feuillard, M., 2011. “La Soufrière de la Guadeloupe : un volcan et un peuple. Jasor (Ed), Pointe-à-Pitre”, pp 246.

3.1 Ground thermal anomaly flux

We used airborne thermal imagery to measure the extent and distribution of these thermal anomalies over the entire volcano. The thermal camera used was an InfraTec VarioCam HD with 640×480 pixels resolution which, combined with a 15 mm focal length lens ($56.1 \times 43.6°$ FOV), gives an instantaneous field of view (IFOV) of 1.65 mrad. The noise equivalent temperature difference, NEΔT, was 0.5 K, meaning that the temperature difference between neighbouring pixels needs to be greater than 0.5 K to be distinguishable. We used an Isotech Calisto calibration oven with blackbody source to calculate the drift of the camera's temperature measurements and applied this to our thermal images.

The airborne thermal survey was conducted on 2019-11-22 with helicopter support provided by the local Civil Protection Service and in pre-dawn conditions. The first images were taken at about 05:40 local time and the survey was completed before sunrise (06:14 local time). The advantage of pre-dawn conditions is that ground heating due to incoming solar radiation is minimised. GPS locations were recorded at 1 Hz using a Garmin 64st for the duration of the flight. Images were acquired through the open door of the helicopter from heights of about 50-300 m above the ground. Weather during the flight was good with exceptional visibility (0% cloud cover), and only very light wind from the North (cf. the predominant tradewinds, les Alizées, blow from the East). Little rain had fallen in the week prior to the survey so the ground surface was dry.

We georeferenced and orthorectified our thermal images using points located on a hill-shaded DEM calculated from Institut Geographique National (IGN) aerial photography, processed using the MicMac photogrammetry software (Rupnik et al., 2017) and orthophotos provided directly by the IGN (Fig. 2). Georeferencing was performed in QGIS using a thin-plate spline transform when the images were taken obliquely, or a Helmert transform for vertically-oriented images. Pixel to physical distance conversions were computed as per Bombrun et al. (2018).

A schematic of the various fluxes seen by the camera is shown in Fig. 3. The effective brightness temperature, T_b, is a function of the incoming fluxes which are functions of the temperature of the objects in the field of view through the Steffan-Boltzmann law, P. The brightness temperature is also affected by reflection of incoming radiation (e.g. L_{sol} and L_{atm} in Fig. 3). The absolute, or kinetic temperature of the ground can thus be expressed as

$$T = \left(\frac{T_{\mathrm{cam}}^4 - T_{\mathrm{atm}}^4 - (1-\tau_g) T_g^4}{\epsilon \tau} \right)^{1/4} \tag{1}$$

where T_{atm} is the brightness temperature of the upper atmosphere, τ_g is the transmissivity of an atmospheric and volcanogenic gas mixture between camera and the ground and ϵ is the emissivity of the ground (Fig. 3).

We converted at-camera (brightness) temperature to absolute temperature by applying Eq. 1. Fumarole plumes and areas outside the region of interest were masked. We calculated τ from the surface-camera distance given by the georeferenced images and GPS location of the camera (e.g. Berk and Hawes, 2017). We took the surface emissivity to be constant for all the heated areas with $\epsilon = 0.95$ in line with that found for other studies on andesitic systems (e.g. Sekioka and Yuhara, 1974; Gaudin et al., 2016).

We note that, although not 100% of the steam condenses before reaching the surface, the remanding flux is typically so low that it can be neglected from our heat budget. Liquid water formed through condensation typically does not reach the surface and either drains away to be output elsewhere in the system (i.e. through thermal springs) or transfers its heat to the ground. Hence we do not consider heat transported by condensed water here (cf. Gaudin et al., 2015). Our heat balance is thus (Sekioka and Yuhara, 1974; Matsushima et al., 2003; Harris, 2013; Mannini et al., 2019)

$$Q_{\text{soil}} = Q_{\text{soil,rad}} + Q_{\text{sol,conv}} \tag{2}$$

$$Q_{\text{soil,rad}} = \epsilon_{\text{soil}}\sigma\left(T^4 - T_{\text{amb}}^4\right) \tag{3}$$

$$Q_{\text{soil,conv}} = Ah_c\left(T - T_{\text{amb}}\right) \tag{4}$$

where T is the ground temperature, A is the heated area, ϵ_{soil} is the soil emissivity, and h_c is the heat transfer coefficient that depends on several factors, particularly the local wind speed, w. In this study we use the Schlichting-Neri model (Neri, 1998)

$$h_c = 1500w(z)\left(1.89 + 1.62\log(z/z_0)\right)^{-2.5}, \tag{5}$$

where z is the height above the surface and z_0 is a measure of the surface roughness. Eq. 5 has been shown to produce results that are consistent with the surface heat balance at La Soufrière de Guadeloupe (Gaudin et al., 2013), such that the heat conducted to the surface equals Q_{soil}. We note that the surfaces on the volcano where heat transfer occurs consist typically of centimetric blocks and thus we take z_0 =0.01 m as our roughness scale. We determined w from measurements at the Sanner weather station (see Fig. 1) at the time of thermal image acquisition. The anemometer at Sanner is approximately 2 m above ground level, so we take $z = 2$ m in our calculations. For wind speeds between 5–10 m/s, as seen on the 22 November, we find h_c between 21.1 and 42.3 $\text{W}/(\text{m}^2\,\text{K})$. Considering error propagation, we estimate a relative standard error of about 10% on the radiative and convective flux measurements, and thus about 15% for the total flux.

3.2 Fumarole heat and mass fluxes

3.2.1 In-plume fumarole steam flux via multigas traverses

The OVSG MultiGAS consists of an IR spectrometer for CO_2 determination and electrochemical sensors for SO_2, H_2S and H_2. The atmospheric pressure (Patm) is determined with the sensor installed on the CO_2 spectrometer card. The MultiGAS also includes an externally-fitted relative humidity (RH) sensor (Galltec, range: 0–100% RH, accuracy: ±2%) and temperature sensor (range: [-30 70]°C, resolution: 0.01 °C), that can be used to determine the concentration of water vapor following the procedure described by Moussallam et al. (2017). H_2O determination with these external sensors allowed us to circumvent the potential influence of steam condensation in the MultiGAS inlet tubing and, therefore, to avoid underestimating the measured water/gas ratios. An onboard GPS receiver tracked the location of the instrument at 1 Hz and the data were visualised on an external tablet connected in real-time via wifi. More detailed information about the OVSG MultiGAS, its design and performance characteristics can be found in Tamburello et al. (2019) and Moretti et al. (2020a,b).

Fumarolic gas fluxes are determined for the three main vents that generate plumes (CS, TAS and G56, Figure 1) following the methodology initially laid out by Allard et al. (2014) and improved upon by Tamburello et al. (2019). The horizontal and vertical distributions of gas species in the plume cross-sections were measured during walking traverses orthogonal to the plume direction, a few meters downwind from the vents. Gas concentrations are measured at two different heights (typically 0.9 and 2 m) as, during most past and current measurements, the volcanic gas plumes are flattened to the ground by strong trade winds (2–14 m/s) and have a maximum height of ca. 3–4 m above the ground at each measuring site with a maximum gas density centered at between 1.5 and 2 m above the ground (our visual observations Gaudin et al., 2016; Tamburello et al., 2019). For each site, we interpolated the concentration measurements using a 2D spline function and then integrated over the plume cross section to obtain integrated concentration amounts (ICAs) using RatioCalc software (Tamburello, 2015). The CO_2 fluxes are derived by multiplying the CO_2 concentration integrated over the plume cross section with the wind speed measured during the gas survey with a hand-held anemometer. We use CO_2 as the volcanic marker to avoid any flux underestimation as it has been shown that, due to its more conservative behavior compared to H_2S and due to the faster response of the IR CO_2 sensor compared to the H_2S chemical sensor, CO_2 sensors are able to detect rapid concentration changes during plume transect which leads to more accurate gas flux measurements (Tamburello et al., 2019). Due to the high atmospheric background for H_2O and CO_2, our walking profiles start and end in pure atmospheric background in order to characterize and then subtract the ambient air composition from our recorded data. Steam fluxes,

$\dot{m}$, are derived from the CO_2 flux by multiplying it by the weight ratio of H_2O/CO_2. Steam flux estimates were possible only when water was successfully determined via the external RH sensor. It is important to note that some variability of steam fluxes could be due to both high ambient humidity on top of the volcano (RH close to 100%), occasional partial steam condensation on the external sensors and rapid weather condition changes at the summit. Indeed, particularly for tropical volcanoes such as La Soufrière de Guadeloupe, water vapour in the plume rapidly condenses upon contact with the atmosphere. However, this condensed water is not taken into account by the MultiGAS measurements. It has been shown that, in such tropical conditions, properly accounting for the condensed water adds approximately 35% to the steam flux estimations (Gaudin et al., 2016), an increase which we consider in our analysis. Lastly, wind speed is the main source of error in quantifying volcanic gas fluxes, leading to typical standard errors on steam flux estimation of about 40%.

3.2.2 At-vent fumarole fluxes via pitot tube measurements

Measurements of the steam exit speed at the vent of several fumaroles were made using a Pitot-tube instrument based around Freescale MPX2200AP and MPX2010DP temperature compensated pressure sensors that measured the dynamic pressure in the moving stream and ambient (stagnation) pressure. Pressure readings were taken at 3.75 Hz and the median of 10 measurements was recorded by an Arduino Due. Uncertainty in the pressure readings was 3.1 Pa, meaning that the minimum recordable speed was about 5 m/s. From these values, the speed of a moving stream of gas, u, of density ρ was calculated as (Massey and Ward-Smith, 1998)

$$u = \sqrt{\frac{2\Delta p}{\rho}} \tag{6}$$

where $\Delta p = p_0 - p$ is the dynamic pressure, p_0 is the stagnation pressure and p is the free-stream pressure. Vent temperatures were simultaneously measured using a PT1000 resistance temperature sensor with an instrumental error of ± 1 K. These measurements, along with the pressure readings, were used to calculate the steam density, $\rho(p, T)$, using numerical codes based on the IAPWS formulation which calculates the Helmholtz energy as a function of temperature and density (Wagner and Pruß, 1993, 2002). Measurements were taken repeatedly at different points across the vent in order to build up an idea of the velocity distribution. The calculations that follow are based on the median velocity from these measurements.

From vent speed, we deduce the mass flux from the fumaroles which, as water vapour contributes up to 98% of the total mass (Allard et al., 2014; Tamburello et al., 2019; Moretti et al., 2020a,

OVSG-IPGP bulletins 2017-2020;), is equivalent to the steam flux,

$$\dot{m} = \rho \bar{u} A \approx \rho_{\text{steam}}(T) \bar{u} A \tag{7}$$

where A is the area of the vent. Whereas in Moretti et al. (2020a) vent area was estimated by eye by the Pitot-tube operator, here we calculate A by analysing thermal images. We repeatedly took thermal images looking straight into the vents throughout the period where Pitot-tube measurements were made, from which we manually traced around the vent perimeter and, using the on-camera laser distance measurements, then converted to physical area (i.e. in m2) via a pixel-to-physical length conversion as per Bombrun et al. (2018). We estimated the relative standard error on mass flux measurements to be 10%.

3.3 Heat flux estimations

The heat released through fumarolic activity is essentially due to cooling and condensation of the volcanic steam. Fumarole heat flux can generally be decomposed into two contributing factors: radiation by the heated vent surface, Q_{rad}, and the specific and latent heat carried by the gas phase, Q_{gas}, so that $Q_{\text{fumarole}} = Q_{\text{rad}} + Q_{\text{gas}}$ (Harris, 2013; Gaudin et al., 2016). Heat lost to the surroundings through the walls of the fumarole pipes is not considered as part of this heat budget, but are accounted for through the geothermal heating of the surrounding ground (Stevenson, 1993; Mannini et al., 2019), as shown in the previous section. Following Harris (2013); Allard et al. (2014); Gaudin et al. (2016) we write these as

$$Q_{\text{rad}} = A \epsilon \sigma \left(T^4 - T_{\text{amb}}^4 \right) \tag{8}$$

$$Q_{\text{gas}} = \dot{m} \left(c_{p,v}(T) \left(T - T_b \right) + L(T) + c_{p,l} \left(T_b - T_{\text{amb}} \right) \right) \tag{9}$$

where ϵ is the ground emissivity, σ is the Stefan-Boltmann constant, c_p is the specific heat capacity of the gas phase, $L \approx 2260\,\text{kJ/(kg K)}$ the latent heat of condensation, T is the temperature of the steam, $T_{\text{b}} \approx 96.7°\text{C}$ is the boiling temperature at the dome altitude and $T_{\text{amb}} \approx 17°\text{C}$ is the ambient temperature at the summit. The subscripts v and l refer to the vapour and liquid states of water, respectively, with $c_{p,v} \approx 2.015\,\text{kJ/(kg K)}$ and $c_{p,l} \approx 4.2\,\text{kJ/(kg K)}$ for summit temperatures and pressures. During the survey period, T ranged from 96.9 and 108.6 °C for CS and has been measured in the water lake at TAS to be approximately 97.5 °C (OVSG-IPGP 2016-2020). Since it is impossible to measure it directly, we estimate that the temperature at the G56 vent is at the boiling temperature of water. We note that c_p and L are functions of p and T and were solved for using similar numerical routines as for density. T_{b} is a function of pressure only and is also deduced from the IAPWS formulations (Wagner and Pruß, 1993, 2002).

Given the instrumental and measurement errors summarised in the text above, and using error propagation techniques (see Gibbings, 1986, for example), we estimated the standard errors on the flux estimation using the Pitot-tube and MultiGAS instruments. In the case of the Pitot-tube instrument, the standard error in estimating Q_{fumarole} is dominated by the mass flux and radiative flux terms and, overall, is of the order of 10%. The standard error for our estimates based on MultiGAS measurements is dominated by the uncertainty in the mass flux measurements alone and so is about 40%.

3.4 Thermal Springs

The nine thermal springs situated around the base of the current dome have been monitored regularly by the OVSG since 1978 by manually measuring temperature and flow rate. The majority of sites have been visited on a 1-3 month basis to take manual temperature readings as well as physico-chemical parameters such as pH and conductivity, and to take samples for future chemical analysis (e.g. Villemant et al., 2005, 2014). During these outings, and when it was possible, volumetric flow rate, $\dot{V}$, was deduced from the time taken to fill a container of known volume. This process was repeated 6-10 times and we report here the mean value of these measurements. From this, we calculate the mass flow rate, $\dot{m_{\text{spring}}} = \rho\dot{V}$, which then allows us to calculate the heat flux as the sum of specific, evaporative and radiative heats,

$$Q_{\text{spring}} = Q_{\text{spec}} + Q_{\text{evap}} + Q_{\text{rad}} \tag{10}$$

$$\text{with} \quad Q_{\text{spec}} = \dot{m} c_{p,l}(T)(T - T_{\text{amb}}) \tag{11}$$

$$Q_{\text{evap}} \propto \chi - \chi_{\text{amb}} \tag{12}$$

and Q_{rad} as per Eq. (8). We note that evapotransport and radiative heat losses contribute negligibly to the heat budget of the thermal springs and so are not included here.

4 Results

4.1 Ground heat flux

We show our results from the analysis of the thermal images (Fig. 2) in Table 1. For each site with detected thermal activity (summit, lower Ravine Matylis, Ravine Claire and FTY), we have determined radiative and convective fluxes as well as the flux density, $q_i = Q_i/A$. As large fluxes can be observed by low intensity emissions over a large area, we also calculate the total heat-flux density, $q = (Q_{\text{rad}} + Q_{\text{conv}})/A_{heated}$, as a metric for comparing intensity between sites (Table 1) with a relative standard error of about 6%. At the summit we found the radiative flux to be

342 0.74 MW and the convective flux to be 4.94 MW, with h_c =41.61 ± 2.26 W/(m^2 K) (Eq. 5) and
343 A_{heated} =14 074 m^2 (Fig. 2). These values were by far the largest in magnitude of all the sites, and
344 larger than the total heat fluxes for the other sites combined. This finding is supported by the
345 heat-flux density, which is considerably greater than any other site.

346 We calculated h_c =37.80 ± 2.26 W/(m^2 K) for wind speeds during acquisition of the images of
347 the flank sites, which was used in the calculations for all sites. Owing to a relatively large emitting
348 surface of 8014 m^2, the heat flux at Ravine Claire (RC) is second to the summit with radiative and
349 convective fluxes of 0.13 MW and 0.75 MW (Table 1), respectively. In the lower Matylis ravine,
350 a strong thermal anomaly leads to high flux densities (41.7 and 238 W/m^2 for radiation a0nd
351 convection, respectively), although a low heated area (1632 m^2) keeps the overall fluxes low. We
352 identified two sites along FTY which have similar results for flux density and had a total flux of
353 0.58 MW and a mean flux density of 226.7 W/m^2. We note that all these sites (Matylis, RC, FTY)
354 are linked to the Ty N-SE and Galion N-S faults that cut the dome (e.g. Komorowski et al., 2005;
355 Rosas-Carbajal et al., 2016).

356 4.2 Fumarole heat and mass flux

357 The mass and heat fluxes are shown in Fig. 4 a) and b), respectively. Steam fluxes estimated
358 from MultiGAS traverses show that, using CO_2 as a marker, the min/mean/max values are:
359 0.35/0.52/0.86, 0.15/0.30/0.47 and 0.29/0.44/0.67 kg/s for CS, G56 and TAS, respectively.

360 Heat flux estimates based on these data give 0.93/1.36/2.28, 0.40/0.79/1.25 and 0.78/1.12/1.79 MW
361 for CS, G56 and TAS, respectively. Considering the relative standard error of 40%, we find that
362 the MultiGAS fluxes have remained stable since regular estimates began in mid 2018, subsequent
363 to the M_L4.1 earthquake.

364 The temporal variations in fumarole steam flux calculated by the Pitot-tube for the three vents
365 at CS are also shown in Fig. 4a. These data indicate that the fluxes can show a large degree of
366 variation in short time periods which is especially true during periods of accelerated unrest such as
367 from March-May 2018 (Moretti et al., 2020a). We find steam fluxes to have min/mean/max values
368 of 0.01/0.12/0.31 kg/s at CSC, 0.22/0.70/1.50 kg/s at CSN and 0.82/2.71/3.85 kg/s at CSS (Fig.
369 4a), which equate to heat fluxes of 0.03/0.29/0.75 MW for CSC vent, 0.53/1.69/3.64 MW for CSN
370 vent, and 1.99/6.56/9.31 MW for CSS vent (Fig. 4b). Fluxes were also measured at NAPN and we
371 found mean mass and heat fluxes of 0.03 kg/s and 0.07 MW with very little variation over time,
372 including during the 2018 unrest. The contribution of NAPN to the total heat and mass budget
373 is thus negligible. We note that, due to an improved method for estimating vent area based on
374 head-on thermal images compared to visual estimation during measurements (see Methods), the
375 vent heat fluxes presented here are quantitatively lower than reported in Moretti et al. (2020a),

although the qualitative temporal variation is the same. The Pitot-tube data show that vent fluxes at CS were strongly affected by and decreased during the 2018 unrest phase, but have since settled to around 4 kg/s and 10 MW for mass and heat flux, respectively. Fig. 4b) shows, although the coefficients for heat capacity and latent heat vary with temperature, the same trends as per Fig. 4a), indicating that the heat flux depended much more strongly on the variations in mass flux than temperature changes during this period.

At CS, we have overlap in the Pitot-tube and MultiGAS instrument data that allows us to compare the data collected by these instruments from closely spaced outings. For example, in terms of steam flux the Pitot-tube data from 2020-06-15 show that CSC+CSN+CSS emitted around 4.6 ± 0.5 kg/s. The flux estimated from MultiGAS measurements at CS on 2020-05-22 were 0.68 ± 0.27 kg/s. These MultiGAS estimates are almost an order of magnitude times lower than those from the Pitot-tube, and Fig. 4 indicates that this is systematically the case. Whilst we have attempted to correct for the quantity of condensed vapour that is undetectable by the MultiGAS, additional errors in this calculation are likely to be primarily responsible for the difference between these two values, although they agree to within an order of magnitude and appear to show qualitatively the same temporal variations.

4.3 Thermal springs heat and mass fluxes

In Fig. 5, we present the mass flow rate and temperature measured over the period between 2000 and 2020 (a subset of the entire dataset, see Villemant et al., 2005, Fig. 5a and b), as well as the heat flux calculated from this via Eqs. (10) (Fig. 5c). Whilst the flow rate and temperature measurements have continued until the present day, there are gaps in the mass and heat flux data during 2014-2016 due to instrument failures. The GA, Tarade spring (TA), Bains Jaunes (BJ) and Pas du Roy (PR) springs are amongst the most accessible and this is reflected in both the abundance and persistence of the measurements in the OVSG database. They are also the most representative of acid-sulfate thermal springs linked to La Soufrière de Guadeloupe's hydrothermal activity. This record does not reflect the absolute total mass/thermal output of the thermal springs as i) other sites are known but are far more inaccessible or impractical to measure and ii) some sites may not yet have been discovered. However, particularly as GA and TA have the largest known flow rates, it is likely that these calculations are nonetheless representative of the total budget for the thermal springs. We fitted linear trends to the data for TA, GA and PR, and extrapolated where necessary to project the values to the current date.

Overall, we see that both mass flow rate and water temperature have slowly and steadily increased over time in an approximately linear fashion. For example, the flow rate at TA increased from around 1.1 kg/s in 2010 to 2.1 kg/s at present whilst its temperature rose from 309 to 318 K

(36 to 45 °C). Only the TA and PR sites have data that cover the whole data range and manual measurements stopped at GA in 2014. Historically, GA dominates the heat budget for the thermal springs, and has almost double the output of TA. Summing over these three sites, we find that the total heat flux from the thermal springs is around 0.57 MW.

5 Discussion

5.1 Comparison of steam and heat flux estimation methods

5.1.1 Fumarole flux

Our measurements (Fig. 6) show that the plume mass and heat fluxes have not undergone extensive evolution since August 2005. With this in mind, we must consider that the fumarole plume heat and mass flux estimates of Gaudin et al. (2016) to be excessively high. In their discussion, the order of magnitude discrepancy with the estimations from MultiGAS traverses (Allard et al., 2014) was mostly attributed to the MultiGAS studies not accounting for condensed water vapour. However, we note several key assumptions in Gaudin et al. (2016) that may have led to systematic errors in their estimations:

- Plume thickness grows with distance from the vent as $\mathcal{H} \sim x$, and not $x^{2/3}$, which is the scaling of the height of the plume axis (e.g. Slawson and Csanady, 1967), so that their mass flux integral overestimates the plume area.
- In calculating plume transmissivity, the plume section is assumed to be axisymmetric. However, this is generally not correct: wind-blown plumes from smoke stacks, cooling towers and in laboratory experiments have been shown to be more broad (horizontally) than thick (vertically, e.g. Contini and Robins, 2001). Thus, calculated plume transmissivity looking horizontally through a plume will be lower than is actually the case and plume temperatures will be higher. Consequently the plume density and thus the mass flow rate will be lower than they estimated.
- The vapour carrying capacity of the plume is assumed to be equal to that of the atmosphere. However, as plume temperatures are higher than atmospheric, and more water vapour can therefore be carried without condensing so this relationship does not hold.

Overall, this suggests that a more realistic plume flux for 2010 would be more in line with the MultiGAS (taking into account condensed vapour) and Pitot-tube measurements, that is a steam flux of 5.3 kg/s for CS. Scaling the flux accordingly for TAS gives 6.2 kg/s. In terms of heat flux, we thus find 13.0 MW for CS and 15.2 MW for TAS (see Table 2).

Moreover, despite some assumptions, our results show that MultiGAS traverses and Pitot-tube measurements provide qualitatively coherent vent flux estimations yet quantifying the steam flux

using MultiGAS is a challenge, particularly in a tropical atmosphere with 100% RH. To overcome this shortcoming, we take the H_2O/CO_2 ratio determined from Giggenbach bottle sampling (OVSG-IPGP 2017-2020; Moretti et al., 2020b) and multiply this by the CO_2 flux estimated from the MultiGAS data. As this ratio is measured at the vent, it is not subject to a loss of matter due to condensation contrary to measurements within the plume. The resulting fluxes at CS ressemble much more closely the Pitot-tube-derived fluxes (see 'Reworked CS MG data' in Fig. 4). This correlation starkly indicates the difficulties in accounting for condensed volcanogenic vapour in the MultiGAS steam-flux estimations. Nevertheless, in a monitoring context, either or both methods could be applied in various volcanoes worldwide to estimate their mass and heat fluxes.

5.1.2 Ground flux

Although we have used the same model for h_c as Gaudin et al. (2016), we obtain slightly different values simply due to differing weather conditions (compare $h_c = 41.61 \pm 2.26$ and $37.80 \pm 2.24\,\mathrm{W/(m^2\,K)}$ for the summit and flanks, respectively, with $h_c = 30.50 \pm 0.31\,\mathrm{W/(m^2\,K)}$ as derived from data in Table 2 of Gaudin et al. (2013). Thus, similarity between the results of our study and those of Gaudin et al. (2013) at the same site would be suggestive of a decrease in temperature at that site. A good comparison can be made at the FTY sites. We note in particular that the mean total heat flux density for FTY0 + FTY1 sites combined, 227.80 W/m2, is in strong agreement with the heat flux density calculated from temperature gradient measurements of $265 \pm 45\,\mathrm{W/m^2}$ (Gaudin et al., 2013), which suggests that, on average, temperatures have not decreased (the ambient temperature during the 2010 survey and ours was approximately 17 °C in both cases). It is somewhat unclear precisely where Gaudin et al. (2016) defined the boundary of FTY and, indeed, their Fig. 1 suggests that this might extend into what we define as Ravine Claire, so judging the evolution of the extent of this site is difficult. However, taking uncertainties into account, the present-day total flux for FTY0+FTY1+RC of 1.46 ± 0.23 MW is not too dissimilar to the 1.0 ± 0.2 MW reported in 2010.

As stated above, images were taken from about 100–300 m above the ground. Given the angular resolution of the thermal camera, this equates to a pixel length of between 0.1 and 0.5 m. As fumaroles are often of smaller dimension than the resolution length-scale, especially when recording from greater distances, their temperature is integrated over the pixel area along with the cooler surroundings and so pixels that cover thermally inhomogeneous ground will display temperatures lower than the true temperature of the hotter object. Harris et al. (2009) demonstrated that, at a distance of 100 m, the pixel-integrated temperature of a 6×13 cm ($78\,\mathrm{cm^2}$) fumarole in a $169\,\mathrm{cm^2}$ pixel was lower than the actual temperature by 40 °C. Taking this into account, we must consider

that the fluxes that we calculate are minimum estimates, emphasising the importance of the ground heat flux for La Soufrière de Guadeloupe.

5.2 Temporal evolution

La Soufrière de Guadeloupe has undergone a significant evolution of its activity in the past decade as described and analyzed in detail by Moretti et al. (2020a) and OVSG-IPGP (2014-2020). This can be summarised as follows:

1. The appearance of new fumarolic vents and the reactivation of pre-existing fumaroles with locally high-velocity degassing.
2. Vegetation die-off near-to and far-from active vents (see Appendix A1).
3. The enlargement of a major extensive area of heated ground on the summit areas that progresses towards the North from the Fracture Napoléon (see below and Appendix A2).
4. More frequent and stronger seismic events including felt events (M_L4.1, April 2018).
5. An acceleration in the opening rate of several summit fractures.
6. The appearance of new mineralised water springs at the base of the volcano as a result of the rapid cooling of hydrothermal fluids.

Undoubtedly the greatest phenomenological change at the summit of La Soufrière de Guadeloupe is indeed the appearance and spread of the ground thermal anomaly in the ZFNN region. For example, the heated area at the summit has gone from an estimated 613 m^2 in 2010 (Gaudin et al., 2016) to 14 074 m^2 for the present study. Indeed, whereas Gaudin et al. (2016) identified thermal anomalies along the Napoléon fracture and in the craters containing the CS fumaroles, they calculated that the associated heat losses were 0.01 MW by radiation and 0.2 MW by forced convection. The present-day radiative and convective fluxes of 0.74 ± 0.07 MW and 4.94 ± 0.49 MW have increased by an order of magnitude in the past decade which is in large part due to this increase in heated area and also, to a lesser degree, because of increased temperatures. The total heat flux density presently estimated at 403 ± 26 W/m^2 is greater than the 2010 estimate of 326.3 ± 68.5 W/m^2, and thus suggests an increase in thermal intensity at the summit, though these values are within the bounds of measurement uncertainty.

Apart from the pulse of unrest around March-April 2018, the fumarolic fluxes have not changed considerably since early 2018 (Fig. 4), and the thermal spring fluxes have increased only slightly (Fig. 5) over the past 20 years. To gain a greater perspective of the overall temporal evolution of plume fluxes over a similar period, we plot in Fig. 6 our data along with the steam and heat fluxes taken from Allard et al. (2014), Gaudin et al. (2016) and Tamburello et al. (2019). This figure shows that our current data are highly consistent with the previous MultiGAS measurements of Allard

et al. (2014) and Tamburello et al. (2019) and also the Pitot-tube measurement for the CSN + CSC vents cited in Gaudin et al. (2016) (compare their value of 5.3 ± 1.6 kg/s to the contemporary sum for CSN + CSC of around 2.0 ± 0.4 kg/s, Fig. 4a).

Three major swarms of VT earthquakes occured from 1 February to 28 April 2018, with the third swarm initiated by the off-volcanic axis $M_L 4.1$ earthquake which struck at 00:32 UTC on 28 April and was widely felt throughout Guadeloupe. In particular, as reported in Moretti et al. (2020a), a short-lived increase in plume flux occurred concurrently with temperature increases before the earthquakes, but both observables had returned to background levels before the $M_L 4.1$ event on 27 April 2018. Hence, our Pitot-tube flux results in particular prove the importance of these flux estimations to monitor closely the volcanic activity.

Our results combined with published data indicate that plume flux has decreased overall since these records began. Thus, given a lack of increased VT seismicity or other signs of sudden evolution in 2010, and in the light of the errors discussed above, it seems that the values reported in Gaudin et al. (2016) are anomalous. In order to provide a better comparison with the present study, we attempt to re-estimate the 2010 plume fluxes given the available data from this period (Allard et al., 2014; Gaudin et al., 2016). We suppose that, despite possible overestimation, the ratio of CS/TAS fluxes was correctly established in 2010 and that the relative standard error will remain unchanged. Thus scaling with the 2005 Pitot-tube data, for 2010 we find steam fluxes of 5.3 ± 1.1 kg/s for CS and 6.2 ± 2.2 kg/s for TAS, and heat fluxes of 13.0 ± 2.6 MW for CS and 15.2 ± 5.4 MW for TAS (Table 2).

In this study, we report thermal spring fluxes derived from a linear regression of the thermal springs time series, we do the same for 2010, calculating these for 2010-02-19, the date of the aerial survey (see Fig. 5). These new values for the thermal springs fluxes are, in general, not appreciably different to the present values, except for TA which we find to be about half the reported value for 2010. Additionally, this process does allow us to calculate fluxes for PR, absent in the 2010 survey. Consequently, we find that the total heat flux in 2010 was likely to have been around 30 MW of which the fumarolic contribution was approximately 28 MW, or 95% of this total. This compares to the estimate of 98% by Gaudin et al. (2016).

The starkest change in the past decade is an increase in ground heat flux by greater than an order of magnitude (see Table 2), reflecting the appearance of the strong and widespread thermal anomaly in the ZFNN area in particular. Indeed, the ground heat flux has increased from 1.2 ± 0.3 MW of a total budget of 29.8 ± 8.3 MW (4%) to 7.6 ± 1.1 MW of 36.5 ± 7.9 MW (21%). Nevertheless, in terms of heat-flux density across the entire edifice, the present-day value of 288.8 ± 88.9 W/m^2 is very similar to 337.1 ± 196.6 W/m^2 in 2010. Going by the values published in Gaudin et al. (2016), fumarole heat flux has quite drastically decreased, going from 28.2 ± 8.0 MW

to 17.8 ± 4.5 MW (excluding G56, Table 2). However, our reanalysis suggests that this change is not so important (28.2 ± 8.0 MW, Table 2 and Fig. 6). Heat transport at the thermal spring sites has increased from 0.4 to 0.6 MW. Taken together, these findings are suggestive of the edifice becoming more fractured and porous over time, allowing some of the hydrothermal fluids to escape via different pathways. The increase in porosity and fracturing may be a result of rock dissolution and weakening (e.g. Pola et al., 2012; Wyering et al., 2014; Heap et al., 2015; Mordensky et al., 2019) as a result of hydrothermal alteration by acid-sulphate fluids (e.g. Salaün et al., 2011). An increase in porosity and fractures is coherent with the increased opening rate of fractures as well as the GNSS radial horizontal displacement (Moretti et al., 2020a) and is corroborated by the appearance of a new thermal mineralized spring at the base of the dome in the upper northern branch of the Matylis river and in the Breislack area (Fig. 1b). Consequently we must expect that the extent and magnitude of thermal anomalies and diffuse degassing on La Soufrière de Guadeloupe will continue to increase over time and, indeed, this is evident in the aerial images shown in Figs. A.1 and A.3 in the supplementary material.

5.3 Total heat budget

As noted by Gaudin et al. (2016), some heat loss may be undetectable by the methods described in this work, due to either vegetation cover (e.g. on the flanks), temperature changes that are below the instrument resolution (cf. summit in the region of CS), or simply being of a form that is undetectable by the temperature sensing equipment used here. As per their work, we note that the "background" heat conducted through the system, as deduced from borehole measurements and extrapolated to the scale of the dome adds an additional 0.013 MW. Furthermore, we note that some heat will be transported not by steam but by other gases, notably CO_2 in the plume and, in particular, CO_2 soil degassing which is a widely-used proxy for heat flux (cf. Chiodini et al., 1998; Bloomberg et al., 2014; Harvey et al., 2015). A detailed study is beyond the scope of this present work but we may make progress under the following assumptions:

1. Passive CO_2 degassing occurs in the same areas and to the same extent as the ground thermal anomalies.
2. The ground heat flux, Q_{sol}, calculated above equals the underground convection of steam, $\dot{m}_{H2O} c_{p,H2O}(T - T_{\mathrm{amb}})$.
3. The CO_2/H2O ratio in areas of soil degassing is the same as in the fumaroles.

Under assumption (2), $\dot{m}_{H2O}$ =135.53 kg/s based on a typical anomaly temperature of 80 °C and ambient temperature of 15 °C. Based on a H_2O/CO_2 ratio of 43.5 (OVSG-IPGP, 2020), this gives $\dot{m}_{CO2}$ =3.15 kg/s and thus $Q_{\mathrm{CO2}} = \dot{m}_{\mathrm{CO2}} c_{\mathrm{p,CO2}}(T - T_{\mathrm{amb}}) = 0.19$ MW.

Clearly, although comparable to the contributions of certain thermal springs, heat transport by CO_2 does not add significantly to the total budget. Nevertheless, due to the accelerating spread of the altered zones and the fact that the area over which CO_2 degassing occurs may be far greater than that involved in degassing of water vapour (cf. Chiodini et al., 2005), the OVSG has begun to carry out joint surveys of soil temperature profiling and CO_2 flux (via the accumulation chamber technique, e.g. Chiodini et al., 1998) in order to further constrain ground heat losses and we will return to this issue in a forthcoming paper.

Summing the fumarole (28.30 ± 6.75 MW, 77.5%), ground (7.60 ± 1.14 MW, 20.8% and the thermal springs fluxes (0.56 MW 1.5%), we obtain a total heat output of 36.5 ± 7.9 MW (see Table 2).

5.4 Comparison with other hydrothermal systems

La Soufrière de Guadeloupe's total heat budget is on par with other major hydrothermal system volcanoes. For example, the heat output at Vulcano (Italy) was estimated at 10–12 MW from combining ground based radiometer and ASTER measurements (Mannini et al., 2019). At Whakaari (NZ), heat output estimated using crater floor soil CO_2 degassing as a proxy was found to be 20.0 ± 2.5 MW (Bloomberg et al., 2014). Our value is somewhat smaller than Nisyros (Greece), Ischia or Campi Flegrei (both Italy) which release in the range of 40–100 MW (Chiodini et al., 2005). However, as noted by Harvey et al. (2015), whilst total heat budget is helpful for following the temporal evolution of an individual volcano, a more useful metric for comparing between systems is the heat flux density as, in many of these cases, the major component of heat flux is through diffuse soil heating so larger systems naturally tend to emit more heat. The mean ground heat flux density (combining radiative and convective fluxes) for the entire La Soufrière de Guadeloupe complex is $289 \pm 19\,W/m^2$ (Table 1) which, if we consider the total heat budget over the total heated area of $26\,279\,m^2$, the mean flux density of the currently active part of the La Soufrière complex climbs to $627 \pm 94\,W/m^2$. Based on the data compiled in Harvey et al. (2015) from heat-flux density calculated from CO_2 flux, this ranks La Soufrière de Guadeloupe amongst the world's most powerful heat producing volcanoes, well above Whakaari (NZ - 205 W/m2), Vulcano ($140\,W/m^2$ Mannini et al., 2019), Campi Flegrei ($118\,W/m^2$ and Nisyros ($19\,W/m^2$), although below Ischia ($764\,W/m^2$). Similar to La Soufrière de Guadeloupe, Vulcano, Whakaari and Ischia are also dome volcanoes and the larger heat flux densities here may indicate optimal steam transport to the surface along high-permeable pathways associated with dome emplacement: Ischia, in particular, has a fumarolic H_2O/CO_2 ratio similar to that at la Soufrière de Guadeloupe, (H_2O/CO_2=147 in 2001, Chiodini et al., 2005). This, due to the very extensive hydrothermal system at La Soufrière de Guadeloupe, indicates the dominance of heat and mass transport by water vapour generated

through the interaction of hot magmatic fluids and the water table. Taken together, especially with respect to the recent evolution at the summit, these findings indicate the importance of ground heating and thermal anomalies as a precursor for unrest of volcanic sites such as La Soufrière de Guadeloupe which may be far more relevant than at caldera-type sites (e.g. Campi Flegrei or Nisyros) where CO_2 degassing is far more pervasive and heat loss through the ground is dominant.

6 Conclusions

La Soufrière de Guadeloupe is an andesitic type stratovolcano in the lesser Antillies arc with an extensive hydrothermal system that has undergone six phreatic/hydrothermal eruptions since 1635 C.E. Here, we have concentrated on using thermal measurements to highlight the changes to the system over the past two decades which cover most of the unrest since its onset in 1992. Direct measurements were made of the temperature and mass flux at the key fumarolic emission sites and at numerous thermal springs linked to the hydrothermal activity of La Soufrière de Guadeloupe, and the ground temperature at sites showing extensive thermal anomalies was determined from airborne thermal imagery. From this and ancillary measurements for ambient conditions, we have deduced heat and mass fluxes as well as heat flux densities. We have compared and discussed our measurements in light of historic data available in the literature and, based on a reinterpretation of previously published data, we deduce that fumarolic output has proportionally decreased from representing 95% of the total heat budget in 2010 to 78% currently whereas ground heating has gone from 4% in 2010 to 21% currently. These changes are explained partly by a slight decrease in fumarolic activity over the past decade but also, and more importantly, that ground thermal anomalies on the summit have propagated significantly in recent years. The present-day radiative and convective heat fluxes in the summit area of 0.74 and 4.94 MW, respectively, have increased by an order of magnitude in the past decade which is in large part due to an increase in heated area and also, to a lesser degree, because of increased temperatures. The total heat flux density presently estimated at $403 \pm 24\,\mathrm{W/m^2}$ is greater than the 2010 estimate of $326 \pm 69\,\mathrm{W/m^2}$, and thus suggests an increase in thermal intensity at the summit, though these values are within the bounds of measurement uncertainty. These changes have occurred concurrently with continued and increasing rates of the opening of fractures on the dome as well as steady horizontal radial displacement of 3-10 mm/year for sites on the dome as measured with GNSS. The thermal spring activity has changed little in 20 years although several of the thermal springs closest to the dome (GA, TA, BJ, PR) have shown since 2000 a steady linear increase of their temperature and heat flux rate.

We find that, in terms of heat-flux density (heat loss per unit area), La Soufrière de Guadeloupe is amongst the most intense emitters of heat for volcanoes worldwide, and that its ranking has

dramatically increased in recent years. Given recent unrest events, our assessments point to the presence of magma at or below the brittle-ductile transition releasing heat and fluids and likely subject to periodic refilling from the deeper parts of the magmatic system. These results are coherent with recent petrological analysis of the volcano's last major magmatic eruption in 1530 C.E. by Pichavant et al. (2018) placing a shallow magma reservoir between a depth of 5 and 8 km as well as the interpretation of the geochemistry of emitted fluids by Villemant et al. (2014) and Moretti et al. (2020a,b) that infer a contribution of deep magmatic gases that trigger periodic transitory heating and pressurisation of the deep hydrothermal system near or slightly above the critical point of water at a depth of about 2-3 km below the summit. Despite the current context of a lack of any evidence for the ascent of magma to very shallow depths, it is important to keep in mind in a hazard perspective, that larger, more frequent, or more intense transitory pulses of hot magmatic gases could exceed the buffering capacity of the hydrothermal system as well as the convective efficiency of heat transfer in a relatively and locally open non-sealed host-rock, bringing the overall system to critical conditions compatible with phreatic/hydrothermal eruptive unrest. Hence, La Soufrière de Guadeloupe remains the subject of continued and enhanced surveillance and research strategies to better understand the origin of unrest and track its dynamic evolution.

Acknowledgements The authors thank the OVSG-IPGP team for logistical support and help with data collection, Pierre Agrinier, and especially Gilbert Hammouya and Olivier Crispi for data collection before 2013. We thank Pascal Allemand and IGN for providing the DEM and orthophotos. We thank the Préfecture de Guadeloupe and the pilots of the Dragon 971 helicopter base in Guadeloupe (Groupement d'hélicoptères de la Sécurité Civile, Ministère de l'Intérieur) for providing helicopter support. We thank the Parc National de Guadeloupe for assistance and authorization to undertake research and monitoring on La Soufrière. We are grateful for help and information from Laurence and Eric Barret (Vert Intense). We thank IPGP for providing a 1-year visiting research position for DEJ as well as for general funding to Observatoires Volcanologiques et Sismologiques (OVS), INSU-CNRS for funding provided by Service National d'Observation en Volcanologie (SNOV), and the Ministère pour la Transition Écologique et Solidaire (MTES) for financial support. This work has been supported by the ANR DOMOSCAN, ANR DIAPHANE, the AO-IPGP 2018 project "Depth to surface propagation of fluid-related anomalies at La Soufrière de Guadeloupe volcano (FWI): timing and implications for volcanic unrest" (coord.: R. Moretti), and the European Union's Horizon 2020 research and innovation programme, under grant agreement No 731070 (EUROVOLC project). This study contributes to the IdEx Université de Paris ANR-18-IDEX-0001, is IPGP contribution number 4164 and is Laboratory of excellence ClerVolc contribution number 426. MJH acknowledges funding via the INSU-CNRS project "Assessing the role of hydrothermal alteration on volcanic hazards".

7 Author Contributions

DEJ collected and analysed the field data, prepared the figures and wrote the manuscript. SM, RM, DG, JCK and VR also collected and analysed field data. All authors contributed in the writing and discussion of the manuscript, and consented to its submission.

Fig. 1: (a) La Soufrière region at 1:10000 scale showing the sites (thermal springs and fumaroles) reported here. (b) zoom of the summit area at 1:5000 scale. Site codes are: Cratère Sud Centre (CSC), Cratère Sud Nord (CSN), Cratère Sud Sud (CSS), Gouffre 56 (G56), Tarissan (TAS), Napoléon Est (NPE), Napoléon Nord (NAPN); Carbet-Echelle (CE), Galion (GA), Tarade (TA), Pas du Roy (PR), Bains Jaunes (BJ) and Ravine Marchand (RM3). The base DEM, hillshading and contours were calculated from an aerial LiDAR survey at 5 m resolution. Road, footpath and waterway information were obtained via the French Government's open data platform (https://www.data.gouv.fr/, accessed 2020-04-16) and from IGN's BDTopo. Geological information is as presented in Lesparre et al. (2012); Brothelande et al. (2014); Moretti et al. (2020a) and references therein.

Fig. 2: Georeferenced thermal images of La Soufrière de Guadeloupe and surroundings taken from the helicopter on 2019-11-22 between 05:40 and 06:14 local time at a) 1:5000 and b) 1:2000 scale showing the summit thermal anomalies. The basemap is the 2017 IGN aerial orthophotograph (BDOrtho). The thermal images are shown in greyscale where white and black denote hot and cold, respectively, although the temperature scale is currently qualitative.

Fig. 3: Conceptual model of the heat flux measured by a thermal camera viewing and displayed as the "brightness" temperature, T_b. The incoming heat fluxes (left) from solar radiation, L_{sol}, and from the atmosphere, L_{atm}, are reflected from the surface in proportion to the surface albedo, α, and $1-\epsilon$, respectively, where ϵ is the emissivity of the surface. For a long-wave infrared sensor such as the thermal camera used here, $\alpha \approx 1-\epsilon$. The emitted radiation of the surface (a function of the surface temperature, T) is added to these reflected fluxes which arrive at the camera having been transmitted through a mixture of atmospheric and volcanogenic gases at temperature, T_g, and having transmissivity, τ.

Fig. 4: Time series of the summit fumarole fluxes since the last quarter of 2017 as estimated from pitot tube and multigas data. Steam fluxes are shown in a) and heat fluxes in b). Vertical grey bars indicate the record of VT earthquakes with M¿2.0 (including felt VTs), which are limited to a sequence in early 2018. To aid interpretation of the pitot tube data, we used a linear smoothing function to produce the curves. The MultiGAS data shown (filled symbols) incorporate the 35% increase in steam flux due to condensation of vapour within the plume. The reworked MultiGAS data correspond to the CO2 flux multiplied by the H2O/CO2 ratio determined from Giggenbach bottle analyses.

A Phenomenological changes

In Figs. A.1 and A.3 we present aerial orthophotographs that show the evolution of the landscape and vegetation on the summit and eastern flank of the volcano.

Fig. 5: Mass flow rate, water temperature and heat flux for the thermal springs monitored by the OVSG for the period from 2000-2020. See text for site codes. The colour code for each site is identical between plots and dashed lines show linear trends for the GA, TA and PR sites. Gaps in the flow rate and flux data in 2014 and 2015/16 were due to instrument failures.

Fig. 6: Long term temporal evolution of the fumarole fluxes from 2005-present. In addition to the present dataset, we also plot Pitot-tube data from March-May 2018 (Moretti et al., 2020a) and 2005, along with thermal camera data 2010 (both Gaudin et al. (2016), MultiGAS data from 2006, 2012 (Allard et al., 2014), and reworked data from 2016-2017 (Tamburello et al., 2019). Grey shading indicates the period covered by the present dataset, as shown in Fig. 4.

Table 1: comparison of radiative and convective fluxes, and heat flux density for the sites around La Soufrière de Guadeloupe in 2019. Note that different values of convective flux are given for comparative purposes, corresponding to the different ways that the heat transfer coefficient has been calculated between studies. In the right-hand column, mean values are given for the flux densities, and total values for all other quantities.

	Summit	Matylis (lower)	Ravine Claire	FTY0	FTY1	Total/Mean
Rad. flux density, $q_{\mathrm{rad}}/[\mathrm{W/m^2}]$	52.39	75.98	49.93	71.54	62.45	54.5
Conv. flux density, $q_{\mathrm{conv}}/[\mathrm{W/m^2}]$	350.78	455.06	310.79	432.52	383.65	350.9
Total heat flux density/$[\mathrm{W/m^2}]$	403.17	531.04	360.72	504.06	446.09	405.5
Radiative flux, $Q_{\mathrm{rad}}/[\mathrm{MW}]$	0.74	0.12	0.40	0.10	0.07	1.4
Convective flux, $Q_{\mathrm{conv}}/[\mathrm{MW}]$	4.94	0.74	2.49	0.63	0.42	9.2
Total $(Q_{\mathrm{rad}} + Q_{\mathrm{conv}})/[\mathrm{MW}]$	5.67	0.87	2.89	0.74	0.49	10.6
Heated area/$[\mathrm{m^2}]$	14,074.15	1,632.00	8,014.00	1,460.25	1,100.75	26,281.1

Table 2: Comparison of the mass and heat flux estimates in 2010 (Gaudin et al., 2016) and for 2020 (present study). Values in parentheses are reworked fluxes which, for 2010, are based on the likely evolution of fumarole fluxes (see Fig. 6) and the thermal springs data (Fig. 5) and for the present-day fumarole estimates are the MultiGAS traverse results scaled to the pitot tube measurements. Dashes indicate that no data was acquired at that site. *Encompasses RC and Matylis.

Flux	Year	Fumaroles				Ground thermal anoma		
		CS	G56	TAS	Total	Summit	FTY	Flanks*
Mass [kg/s]	2010	19.5 ± 4.0 (5.3 ± 1.1)	-	22.8 ± 8.1 (6.2 ± 2.2)	42.3 ± 12.1 (11.5 ± 3.3)	-	-	-
	2020	4.89 ± 0.49	(2.09 ± 0.84)	(2.83 ± 1.13)	(9.81 ± 2.45)	-	-	-
Heat [MW]	2010	48.0 ± 9.8 (13.0 ± 2.6)	-	56.1 ± 19.9 (15.2 ± 5.4)	104.1 ± 20.7 (28.2 ± 8.0)	0.2 ± 0.1	1.0 ± 0.2	-
	2020	15.25 ± 1.53	(5.54 ± 2.22)	(7.51 ± 3.00)	(28.30 ± 6.75)	5.68 ± 0.85	0.58 ± 0.09	1.34 ± 0.2

A.1 Summit

On the summit, we see a large extent of barren ground approximately delimited by TAS to the north, G56 to the east and extending south of CS, due to acid gas emissions from the main fumaroles that began in 1992 (OVSG-IPGP 1999-2020; Fig. A.1; Komorowski et al., 2005). To the north of this, delimited by a light blue polygon in Fig. A.1 and Fig. 2, is an area that has shown significant hydrothermal alteration since 2004, but that became especially visible between 2013 and 2017 (ZFNN). These most recent changes were concomitant with the appearance of the NAPN and NPE high-flux fumaroles in 2014 and 2016, respectively, as well as numerous, small and low flux fumaroles (OVSG-IPGP 2014-2020). Fig. A.2 shows the extent of the fumarolic activity at the summit (excluding CS), taken at an altitude of 1534 m (c.100 m above the ground) and approximately normal to the surface. We further see the extent of ground heating in the hydrothermally altered region, and major and minor fumaroles including CS, TAS, G56, NAPN, NPE1-3 and NAP. From Figs. A.1 and A.2, it is apparent that the thermal anomalies extend towards and into Cratère Dupuy and also into the (currently) vegetated area to the North of ZFNN. (This is also seen in the thermal gradient data, Fig A2-1). We also see extensive heating on the walls of the NAP/Peysonnel fracture. Finally, vegetation surrounding the G56 site has suffered significant die off, presumably due to the strongly acidic gases emitted since 2007. Though no signs of unrest appear in the 2010 imagery, the changes seen in these images are consistent with the reported phenomenological evolution (OVSG-IPGP 2010-2020).

Despite the barren landscape to the south of ZFNN, no signs of ground heating are seen in the aerial imagery. This is confirmed by thermocouple measurements made in April 2019 though, historically, ground thermal anomalies

Fig. A.1: Evolution of ground alteration in the Breislack region from IGN aerial photography (https://remonterletemps.ign.fr/). Images are oriented with the North upwards.

Fig. A.2: quasi-vertical zoomed uncalibrated thermal image of the main summital temperature anomaly (ZFNN) and surrounding features. Brightness of the pixels is a proxy for temperature.

Fig. A.3: Evolution of ground alteration in the Faille de la Ty/Matylis/Galion region from IGN aerial photography (https://remonterletemps.ign.fr/). Images are oriented with the North vertically up

Fig. B.1: Near-surface temperature profiles and temperature gradients as measured in 2001 and April 2019, respectively.

have been found between the Lacroix fractures and CS (Figs. 1 and B.1), whose absence in the current survey is suggestive of a sealing effect in the southern half of the summit.

A.2 Flank activity

On the eastern flank of La Soufrière de Guadeloupe, the Breislack fracture (an extension of the Peysonnel/Napoléon/Lacroix fractures) and surrounding area shows clear signs of hydrothermal alteration in recent years (Fig. A.3). Vegetation die off, presumably due to diffuse degassing of CO2, has been observed since at least March 2015, although we do not currently find signs of a ground thermal anomaly. In January 2019 we observed a thermal anomaly of 1 °C (cf. camera NEΔT 0.5 °C) in the interior of the Breislack fracture along with some minor whitish sublimates in the fracture's interior, concomitant with elevated CO2 levels. However, the thermal anomaly was absent and CO2 concentrations were indistinguishable from background levels when the site was revisited in May 2020. Previously established hydrothermally altered areas devoid of any thermal anomaly such as the Col de l'Echelle, last active in 1984 (Komorowski et al., 2005), have not changed in recent years.

To the south of the volcano, FTY and RC are sites with strong alteration and thermal anomalies which do not appear to have evolved in the past decade (see Figs. 5 and A1-3). Our thermal images show that the road and the more evident sulphur-bearing slopes are heated. The upper Matylis ravine is cold, as observed by direct temperature measurements in January 2019, though we have observed elevated levels of CO2 (mean 700 ppm, max 1500 ppm) on several visits to this site (OVSG-IPGP 2014-2020). A strong thermal anomaly is present in the lower Matylis ravine. The Galion ravine with its twin hot-springs is clearly visible in the thermal imagery (Fig. 2) and appears not to have evolved since 2010.

B Near surface temperature profiles and gradients

In April 2019, in preparation for the installation of a distributed temperature sensor (see Jessop et al., 2019), a series of shallow boreholes were dug across a major part of the summit up to a depth of 80 cm. During this process, the temperature was logged at several depths (typically 20, 40 and 80 cm). From this data, using the temperature difference at the two deepest points, we have derived the near-surface temperature gradient at each site, which is shown in Fig. B.1. This data shows clearly the cooling of the surface between CS and LCX (up to 95 °C in 2001) and the present day, and the warming of the northern half of the dome (north of NAP). See Fig. 1 for site names.

References

Allard, P., Aiuppa, A., Beauducel, F., Gaudin, D., di Napoli, R., Calabrese, S., Parello, F., Crispi, O., Hammouya, G., Tamburello, G., 2014. Steam and gas emission rate from la Soufrière volcano, guadeloupe (lesser antilles): implications for the magmatic supply during degassing unrest. Chem. Geol. 384, 76–93.

Aubert, M., 10 1999. Practical evaluation of steady heat discharge from dormant active volcanoes: case study of Vulcarolo fissure (Mount Etna, Italy). J. Volcanol. Geoth. Res. 92 (3–4), 413–429.

Aubert, M., Auby, R., Bourlet, F., Y, B., 1984. Contribution à la surveillance de l'activité de l'Etna à partir de l'étude des zones fumerolliennes. Bull. Volcanol. 47 (4), 1039–1050.

Berk, A., Hawes, F., 2017. Validation of MODTRAN®6 and its line-by-line algorithm. J. Quant. Spectrosc. Ra. 203, 542–556.

Bloomberg, S., Werner, C., Rissmann, C., Mazot, A., Horton, T., Gravley, D., Kennedy, B., Oze, C., 2014. Soil CO2 emissions as a proxy for heat and mass flow assessment, Taupō Volcanic Zone, New Zealand. Geochemistry, Geophysics, Geosystems 15 (12), 4885–4904.

Boichu, M., Villemant, B., Boudon, G., 2011. Degassing at La Soufrière de Guadeloupe volcano (Lesser Antilles) since the last eruptive crisis in 1975–77: result of a shallow magma intrusion? J. Volcanol. Geoth. Res. 203 (3), 102–112.

Bombrun, M., Jessop, D. E., Harris, A. J. L., Barra, V., 2018. An algorithm for the detection and characterisation of volcanic plumes using thermal camera imagery. J. Volcanol. Geoth. Res. 352, 26–37.

Boudon, G., Komorowski, J.-C., Villemant, B., Semet, M. P., 2008. A new scenario for the last magmatic eruption of La Soufrière of Guadeloupe (Lesser Antilles) in 1530 AD: evidence from stratigraphy, radiocarbon dating and magmatic evolution of erupted products. J. Volcanol. Geoth. Res. 178 (3), 474–490.

Brombach, T., Marini, L., Hunziker, J., 2000. Geochemistry of the thermal springs and fumaroles of Basse-Terre Island, Guadeloupe, Lesser Antilles. Bull. Volcanol. 61 (7), 477–490.

Brothelande, E., Finizola, A., Peltier, A., Delcher, E., Komorowski, J.-C., Di Gangi, F., Borgogno, G., Passarella, M., Trovato, C., Legendre, Y., 2014. Fluid circulation pattern inside La Soufrière volcano (Guadeloupe) inferred from combined electrical resistivity tomography, self-potential, soil temperature and diffuse degassing measurements. J. Volcanol. Geoth. Res. 288, 105–122.

Chiodini, G., Cioni, R., Guidi, M., Raco, B., Marini, L., 1998. Soil CO2 flux measurements in volcanic and geothermal areas. Appl. Geochem. 13 (5), 543–552.

Chiodini, G., Frondini, F., Cardellini, C., Granieri, D., Marini, L., Ventura, G., 2001. CO2 degassing and energy release at Solfatara volcano, Campi Flegrei, Italy. J. Geophys. Res.-Solid Earth 106 (B8), 16213–16221.

Chiodini, G., Granieri, D., Avino, R., Caliro, S., Costa, A., Werner, C., 2005. Carbon dioxide diffuse degassing and estimation of heat release from volcanic and hydrothermal systems. J. Geophys. Res.-Solid Earth 110 (B8).

Contini, D., Robins, A., 2001. Water tank measurements of buoyant plume rise and structure in neutral crossflows. Atmos. Environ. 35 (35), 6105–6115.

de Vries, B. v. W., Kerle, N., Petley, D., 02 2000. Sector collapse forming at Casita volcano, Nicaragua. Geology 28 (2), 167–170.

Di Renzo, V., Wohletz, K., Civetta, L., Moretti, R., Orsi, G., Gasparini, P., 2016. The thermal regime of the Campi Flegrei magmatic system reconstructed through 3D numerical simulations. J. Volcanol. Geoth. Res. 328, 210–221.

Feuillard, M., Allegre, C., Brandeis, G., Gaulon, R., Mouel, J. L., Mercier, J., Pozzi, J., Semet, M., 1983. The 1975–1977 crisis of la Soufrière de Guadeloupe (f.w.i): a still-born magmatic eruption. J. Volcanol. Geoth. Res. 16 (3), 317–334.

Fischer, T. P., Chiodini, G., 2015. Volcanic, magmatic and hydrothermal gases. In: The encyclopedia of volcanoes. Elsevier, pp. 779–797.

771 Gaudin, D., Beauducel, F., Allemand, P., Delacourt, C., Finizola, A., 2013. Heat flux measurement from thermal
772 infrared imagery in low-flux fumarolic zones: example of the Ty fault (la Soufrière de Guadeloupe). J. Volcanol.
773 Geoth. Res. 267 (0), 47–56.
774 Gaudin, D., Beauducel, F., Coutant, O., Delacourt, C., Richon, P., de Chabalier, J.-B., Hammouya, G., 2016. Mass
775 and heat flux balance of La Soufrière volcano (Guadeloupe) from aerial infrared thermal imaging. J. Volcanol.
776 Geoth. Res. 320, 107–116.
777 Gaudin, D., Finizola, A., Delcher, E., Beauducel, F., Allemand, P., Delacourt, C., Brothelande, E., Peltier, A.,
778 Di Gangi, F., 2015. Influence of rainfalls on heat and steam fluxes of fumarolic zones: six months records along
779 the Ty Fault (Soufrière of Guadeloupe, Lesser Antilles). J. Volcanol. Geoth. Res. 302, 273–285.
780 Gibbings, J. C., 1986. The systematic experiment, first edition Edition. Cambridge University Press.
781 Giggenbach, W. F., 03 1975. A simple method for the collection and analysis of volcanic gas samples. Bull. Volcanol.
782 39, 132–145.
783 Hardee, H. C., 1982. Permeable convection above magma bodies. Tectonophysics 84 (2–4), 179–195.
784 Harris, A. J. L., 2013. Thermal remote sensing of active volcanoes: a user's manual. Cambridge University Press.
785 Harris, A. J. L., Lodato, L., Dehn, J., Spampinato, L., 2009. Thermal characterization of the Vulcano fumarole field.
786 Bull. Volcanol. 71 (4), 441–458.
787 Harris, A. J. L., Maciejewski, A. J. H., 2000. Thermal surveys of the vulcano fossa fumarole field 1994-1999: evidence
788 for fumarole migration and sealing. J. Volcanol. Geoth. Res. 102 (1–2), 119–147.
789 Harris, A. J. L., Stevenson, D. S., 1997. Thermal observations of degassing open conduits and fumaroles at Stromboli
790 and Vulcano using remotely sensed data. J. Volcanol. Geoth. Res. 76 (3–4), 175–198.
791 Harvey, M. C., Rowland, J. V., Chiodini, G., Rissmann, C. F., Bloomberg, S., Hernández, P. A., Mazot, A., Viveiros,
792 F., Werner, C., 2015. Heat flux from magmatic hydrothermal systems related to availability of fluid recharge. J.
793 Volcanol. Geoth. Res. 302, 225–236.
794 Heap, M. J., Kennedy, B. M., Pernin, N., Jacquemard, L., Baud, P., Farquharson, J. I., Scheu, B., Lavallée, Y., Gilg,
795 H. A., Letham-Brake, M., Mayer, K., Jolly, A. D., Reuschlé, T., Dingwell, D. B., 2015. Mechanical behaviour and
796 failure modes in the Whakaari (White Island volcano) hydrothermal system, New Zealand. J. Volcanol. Geoth.
797 Res. 295, 26–42.
798 Heap, M. J., Kushnir, A. R., Vasseur, J., Wadsworth, F. B., Harlé, P., Baud, P., Kennedy, B. M., Troll, V. R.,
799 Deegan, F. M., 2020. The thermal properties of porous andesite. J. Volcanol. Geoth. Res. 398, 106901.
800 Heap, M. J., Troll, V. R., Kushnir, A. R. L., Gilg, H. A., Collinson, A. S. D., Deegan, F. M., Darmawan, H.,
801 Seraphine, N., Neuberg, J., Walter, T. R., 2019. Hydrothermal alteration of andesitic lava domes can lead to
802 explosive volcanic behaviour. Nat. Commun. 10 (1), 5063.
803 Hedenquist, J., Lowenstern, J., 1994. The role of magmas in the formation of hydrothermal ore-deposits. Nature
804 370 (6490), 519–527.
805 Hincks, T. K., Komorowski, J.-C., Sparks, S. R., Aspinall, W. P., 2014. Retrospective analysis of uncertain eruption
806 precursors at la Soufrière volcano, Guadeloupe, 1975–77: volcanic hazard assessment using a Bayesian Belief
807 Network approach. J. Appl. Volcanol. 3 (1), 1–26.
808 Jessop, D. E., Moretti, R., Moune, S., Bonifacie, M., Burtin, A., de Chabalier, J.-B., Deroussi, S., Komorowski, J.-C.,
809 Rosas-Carbajal, M., Bosson, A., Didier, T., Kitou, T., Lemarchand, A., Robert, V., 2019. Les risques volcaniques
810 au XXIe siècle : surveiller et prévoir: l'exemple de l'OVSG. Géologues, 82–90.
811 John, D. A., Sisson, T. W., Breit, G. N., Rye, R. O., Vallance, J. W., 2008. Characteristics, extent and origin of
812 hydrothermal alteration at Mount Rainier Volcano, Cascades Arc, USA: implications for debris-flow hazards and
813 mineral deposits. J. Volcanol. Geoth. Res. 175 (3), 289–314.

814 Komorowski, J., Boudon, G., Antenor-Habazac, C., Hammouya, G., Semet, M., David, J., Beauducel, F., Cheminée,
815 J., Feuillard, M., 2001. L'activité éruptive et non-éruptive de la Soufrière de Guadeloupe: problèmes et implications
816 de la phénoménologie et des signaux actuellement enregistrés (French). Eruptive and non-eruptive activity from
817 La Soufrière of Guadeloupe: problems and implications posed by the current phenomenology and monitoring
818 signals. Workshop on volcanic hazards - Lesser Antilles volcanoes: from processes to signals. In: INSU Lesser
819 Antilles Volcanic Hazard Workshop, Paris. pp. 18–19.
820 Komorowski, J.-C., Boudon, G., Semet, M., Beauducel, F., Anténor-Habazac, C., Bazin, S., Hammouya, G., 2005.
821 Guadeloupe. In: Lindsay, J., Robertson, R., Shepherd, J., Ali, S. (Eds.), Volcanic hazard atlas of the Lesser
822 Antilles. pp. 65–102.
823 Lardy, M., Tabbagh, A., 1999. Measuring and interpreting heat fluxes from shallow volcanic bodies using vertical
824 temperature profiles: a preliminary test. Bull. Volcanol. 60 (6), 441–447.
825 Legendre, Y., 2012. Reconstruction fine de l'histoire éruptive et scenarii éruptifs à la soufrière de guadeloupe : vers
826 un modèle intégré de fonctionnement du volcan. Ph.D. thesis, IPGP, 2012PA077065.
827 Lesparre, N., Gibert, D., Marteau, J., Komorowski, J.-C., Nicollin, F., Coutant, O., 2012. Density muon radiogra-
828 phy of La Soufrière of Guadeloupe volcano: comparison with geological, electrical resistivity and gravity data.
829 Geophysical Journal International 190 (2), 1008–1019.
830 López, D. L., Williams, S. N., 1993. Catastrophic volcanic collapse: relation to hydrothermal processes. Science
831 260 (5115), 1794–1796.
832 Mannini, S., Harris, A. J. L., Jessop, D. E., Chevrel, M. O., Ramsey, M. S., 2019. Combining ground- and ASTER-
833 based thermal measurements to constrain fumarole field heat budgets: the case of Vulcano Fossa 2000-2019.
834 Geophys. Res. Lett.
835 Massey, B., Ward-Smith, J., 1998. Mechanics of fluids, seventh Edition. Stanley Thornes ltd., p. 383.
836 Matsushima, N., Kazahaya, K., Saito, G., Shinohara, H., 2003. Mass and heat flux of volcanic gas discharging
837 from the summit crater of Iwodake volcano, Satsuma-Iwojima, Japan, during 1996-1999. J. Volcanol. Geoth. Res.
838 126 (3–4), 285–301.
839 Mordensky, S. P., Heap, M. J., Kennedy, B. M., Gilg, H. A., Villeneuve, M. C., Farquharson, J. I., Gravley, D. M.,
840 2019. Influence of alteration on the mechanical behaviour and failure mode of andesite: implications for shallow
841 seismicity and volcano monitoring. Bull. Volcanol. 81 (8), 44.
842 Moretti, R., Komorowski, J.-C., Ucciani, G., Moune, S., Jessop, D., de Chabalier, J.-B., Beauducel, F., Bonifacie,
843 M., Burtin, A., Vallée, M., Deroussi, S., Robert, V., Gibert, D., Didier, T., Kitou, T., Feuillet, N., Allard,
844 P., Tamburello, G., Shreve, T., Saurel, J.-M., Lemarchand, A., Rosas-Carbajal, M., Agrinier, P., Friant, A. L.,
845 Chaussidon, M., 2020a. The 2018 unrest phase at La Soufrière of Guadeloupe (French West Indies) andesitic
846 volcano: scrutiny of a failed but prodromal phreatic eruption. J. Volcanol. Geoth. Res., 106769.
847 Moretti, R., Moune, S., Robert, V., Jessop, D. E., Didier, T., Bonifacie, M., Kitou, T., Komorowski, J.-C., 2020b.
848 Intercomparison of geochemical techniques at La Soufrière de Guadeloupe (FWI) volcano: their advantages and
849 their limits over a long-standing unrest. Ital. J. Geosci.
850 Moretti, R., Stefansson, A., 2020. Volcanic and geothermal redox engines. Elements 16, 179–184.
851 Moussallam, Y., Tamburello, G., Peters, N., Apaza, F., Schipper, C. I., Curtis, A., Aiuppa, A., Masias, P., Boichu,
852 M., Bauduin, S., et al., 2017. Volcanic gas emissions and degassing dynamics at Ubinas and Sabancaya volcanoes;
853 implications for the volatile budget of the central volcanic zone. J. Volcanol. Geoth. Res. 343, 181–191.
854 Neri, A., 1998. A local heat transfer analysis of lava cooling in the atmosphere: application to thermal diffusion-
855 dominated lava flows. J. Volcanol. Geoth. Res. 81 (3), 215–243.
856 Pichavant, M., Poussineau, S., Lesne, P., Solaro, C., Bourdier, J. L., 2018. Experimental parametrization of magma
857 mixing: application to the AD 1530 eruption of La Soufrière, Guadeloupe (Lesser Antilles). J. Petrol. 59 (2),

257–282.

Pola, A., Crosta, G., Fusi, N., Barberini, V., Norini, G., 2012. Influence of alteration on physical properties of volcanic rocks. Tectonophysics 566-567, 67–86.

Reid, M. E., 05 2004. Massive collapse of volcano edifices triggered by hydrothermal pressurization. Geology 32 (5), 373–376.

Reid, M. E., Sisson, T. W., Brien, D. L., 09 2001. Volcano collapse promoted by hydrothermal alteration and edifice shape, Mount Rainier, Washington. Geology 29 (9), 779–782.

Rosas-Carbajal, M., Komorowski, J.-C., Nicollin, F., Gibert, D., 2016. Volcano electrical tomography unveils edifice collapse hazard linked to hydrothermal system structure and dynamics. Sci. Rep. 6.

Rupnik, E., Daakir, M., Pierrot Deseilligny, M., 2017. MicMac – a free, open-source solution for photogrammetry. Open Geospatial Data, Software and Standards 2 (1), 14.

Ruzié, L., Aubaud, C., Moreira, M., Agrinier, P., Dessert, C., Gréau, C., Crispi, O., 2013. Carbon and helium isotopes in thermal springs of la Soufrière volcano (Guadeloupe, Lesser Antilles): implications for volcanological monitoring. Chemical Geology 359, 70–80.

Salaün, A., Villemant, B., Gérard, M., Komorowski, J.-C., Michel, A., 2011. Hydrothermal alteration in andesitic volcanoes: trace element redistribution in active and ancient hydrothermal systems of Guadeloupe (Lesser Antilles). J. Geochem. Explor. 111 (3), 59–83.

Sekioka, M., Yuhara, K., 1974. Heat flux estimation in geothermal areas based on the heat balance of the ground surface. J. Geophys. Res.-Solid Earth 79 (14), 2053–2058.

Sigurdsson, H., Houghton, B., McNutt, S., Rymer, H., Stix, J. (Eds.), 2015. The Encyclopedia of Volcanoes. Elsevier Science.

Slawson, P. R., Csanady, G. T., 1967. On mean path buoyant bent-over chimney plumes. J. Fluid Mech. 28 (Part 2), 311–&.

Stevenson, D. S., 1993. Physical models of fumarolic flow. J. Volcanol. Geoth. Res. 57 (3–4), 139–156.

Stimac, J., Goff, F., Goff, C. J., 2015. Intrusion-related geothermal systems. In: Sigurdsson, H., Houghton, B., McNutt, S., Rymer, H., Stix, J. (Eds.), The Encyclopedia of Volcanoes, second edition Edition. Academic Press, Amsterdam, Ch. 46, pp. 799–822.

Tamburello, G., 2015. Ratiocalc: software for processing data from multicomponent volcanic gas analyzers. Comp. Geosci. 82, 63–67.

Tamburello, G., Moune, S., Allard, P., Venugopal, S., Robert, V., Rosas-Carbajal, M., Deroussi, S., Kitou, G.-T., Didier, T., Komorowski, J.-C., Beauducel, F., De Chabalier, J.-B., Le Marchand, A., Le Friant, A., Bonifacie, M., Dessert, C., Moretti, R., 2019. Spatio-temporal relationships between fumarolic activity, hydrothermal fluid circulation and geophysical signals at an arc volcano in degassing unrest: la Soufrière of Guadeloupe (French West Indies). Geosci. 9 (11).

Villemant, B., Hammouya, G., Michel, A., Semet, M. P., Komorowski, J. C., Boudon, G., Cheminee, J. L., 2005. The memory of volcanic waters: shallow magma degassing revealed by halogen monitoring in thermal springs of La Soufriére volcano (Guadeloupe, Lesser Antilles). Earth Planet. Sci. Let. 237 (3–4), 710–728.

Villemant, B., Komorowski, J., Dessert, C., Michel, A., Crispi, O., Hammouya, G., Beauducel, F., Chabalier, J.-B. D., 2014. Evidence for a new shallow magma intrusion at La Soufrière of Guadeloupe (Lesser Antilles): insights from long-term geochemical monitoring of halogen-rich hydrothermal fluids. J. Volcanol. Geoth. Res. 285, 247–277.

Wagner, W., Pruß, A., 1993. International equations for the saturation properties of ordinary water substance. Revised according to the International Temperature Scale of 1990. Addendum to J. Phys. Chem. Ref. Data 16, 893 (1987). J. Phys. Chem. Ref. Data 22 (3), 783–787.

901 Wagner, W., Pruß, A., 2002. The IAPWS formulation 1995 for the thermodynamic properties of ordinary water
902 substance for general and scientific use. J. Phys. Chem. Ref. Data 31 (2), 387–535.
903 Wyering, L., Villeneuve, M., Wallis, I., Siratovich, P., Kennedy, B., Gravley, D., Cant, J., 2014. Mechanical and
904 physical properties of hydrothermally altered rocks, taupo volcanic zone, new zealand. J. Volcanol. Geoth. Res.
905 288, 76–93.
906 Zlotnicki, J., Boudon, G., Mouël, J.-L. L., 1992. The volcanic activity of la Soufrière of Guadeloupe (Lesser Antilles):
907 structural and tectonic implications. J. Volcanol. Geoth. Res. 49 (1), 91–104.

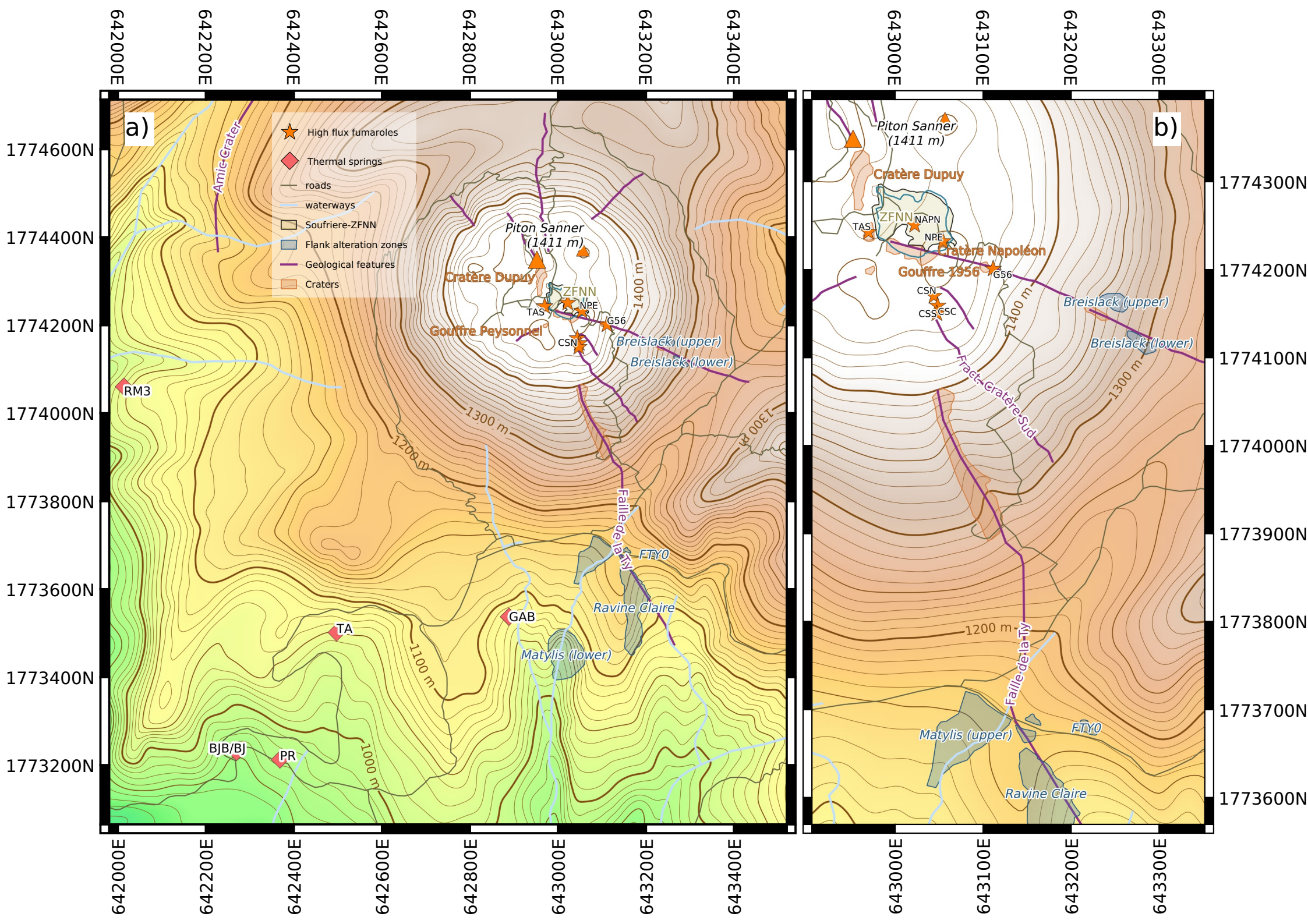
a)
b)
High flux fumaroles
Thermal springs
roads
waterways
Soufriere-ZFNN
Flank alteration zones
Geological features
Craters
Amic Crater
Piton Sanner
(1411 m)
Cratère Dupuy
ZFNN
TAS
NPE
NAPN
G56
Gouffre Peysonnel
Gouffre 1956
Cratère Napoléon
CSN
CSS
CSC
Breislack (upper)
Breislack (lower)
Fracture Cratère Sud
Faille de la Ty
FTY0
Ravine Claire
Matylis (lower)
Matylis (upper)
RM3
TA
GAB
BJB/BJ
PR
1400 m
1300 m
1200 m
1100 m
1000 m
642000E
642200E
642400E
642600E
642800E
643000E
643200E
643400E
643100E
643300E
1774600N
1774400N
1774200N
1774000N
1773800N
1773600N
1773400N
1773200N
1774300N
1774100N
1773900N
1773700N

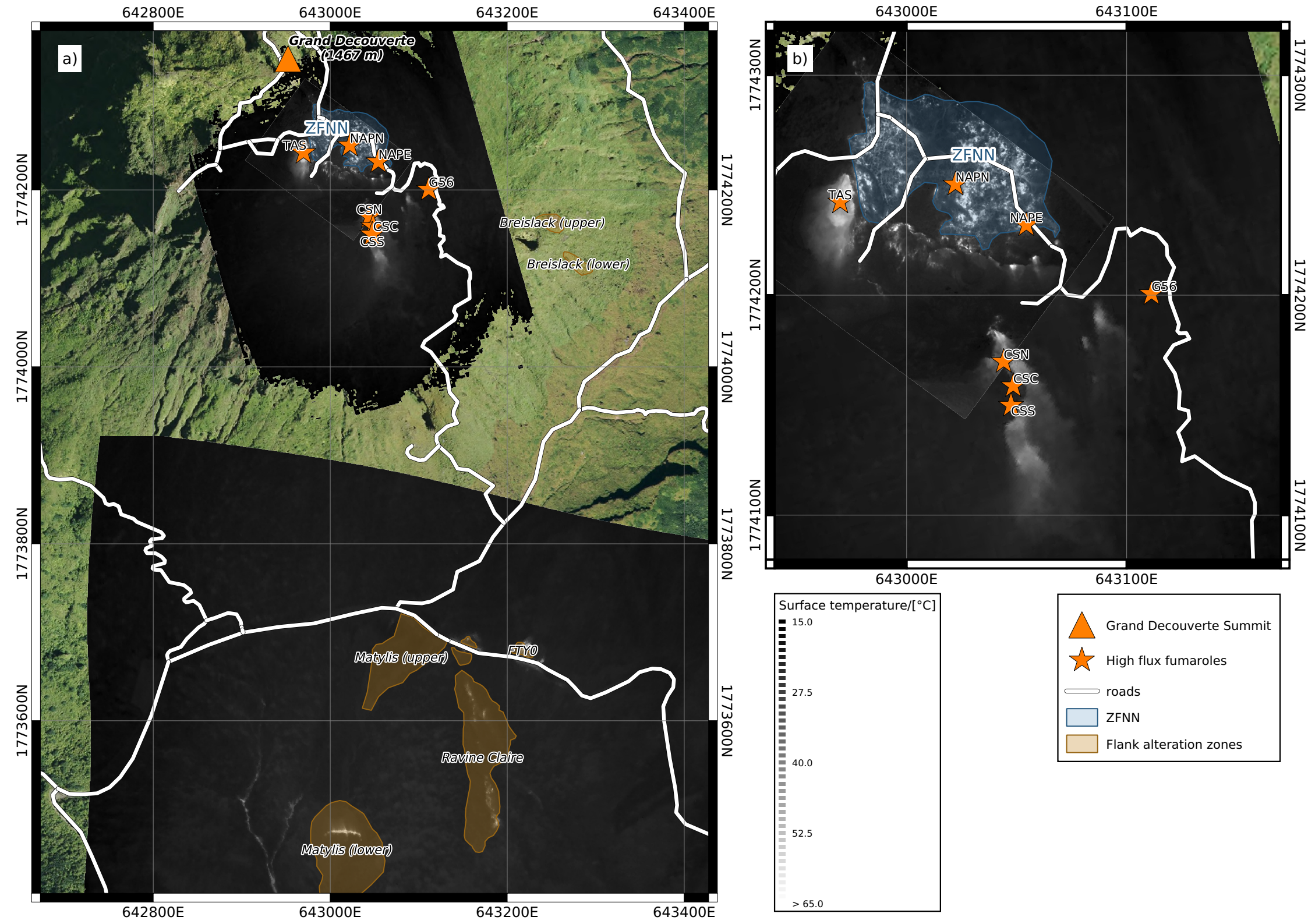
a)
b)
Grand Decouverte (1467 m)
ZFNN
TAS
NAPN
NAPE
G56
CSN
CSC
CSS
Breislack (upper)
Breislack (lower)
Matylis (upper)
FTY0
Ravine Claire
Matylis (lower)
642800E
643000E
643200E
643400E
643100E
1774300N
1774200N
1774100N
1774000N
1773800N
1773600N
Surface temperature/[°C]
15.0
27.5
40.0
52.5
> 65.0
Grand Decouverte Summit
High flux fumaroles
roads
ZFNN
Flank alteration zones

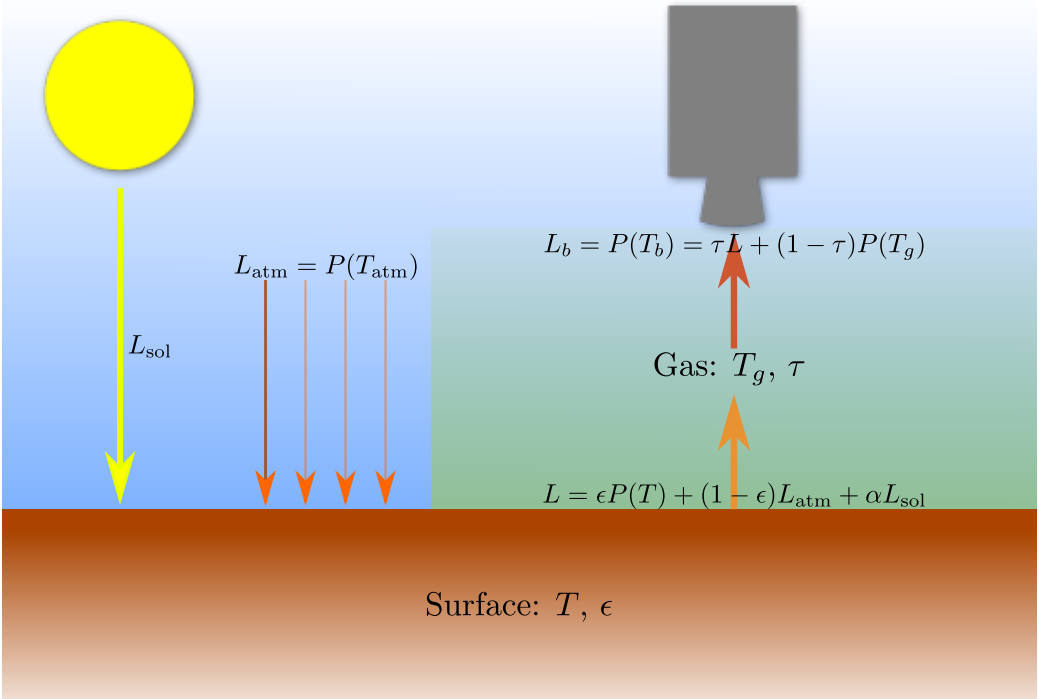
L_{sol}
$L_{\text{atm}} = P(T_{\text{atm}})$
$L_b = P(T_b) = \tau L + (1-\tau)P(T_g)$
Gas: T_g, τ
$L = \epsilon P(T) + (1-\epsilon)L_{\text{atm}} + \alpha L_{\text{sol}}$
Surface: T, ϵ

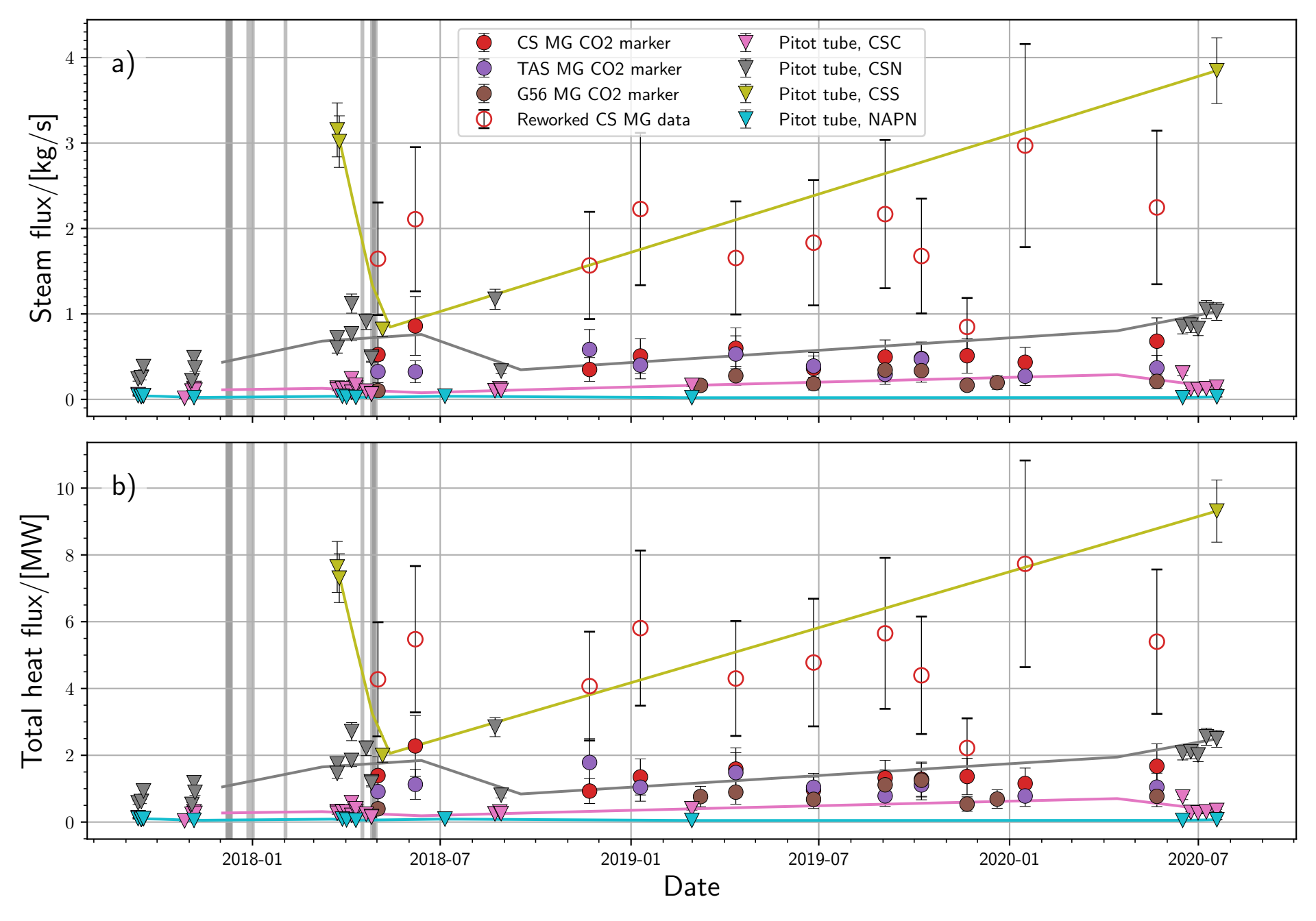
a)
b)
CS MG CO2 marker
TAS MG CO2 marker
G56 MG CO2 marker
Reworked CS MG data
Pitot tube, CSC
Pitot tube, CSN
Pitot tube, CSS
Pitot tube, NAPN
Steam flux/[kg/s]
Total heat flux/[MW]
Date
2018-01
2018-07
2019-01
2019-07
2020-01
2020-07

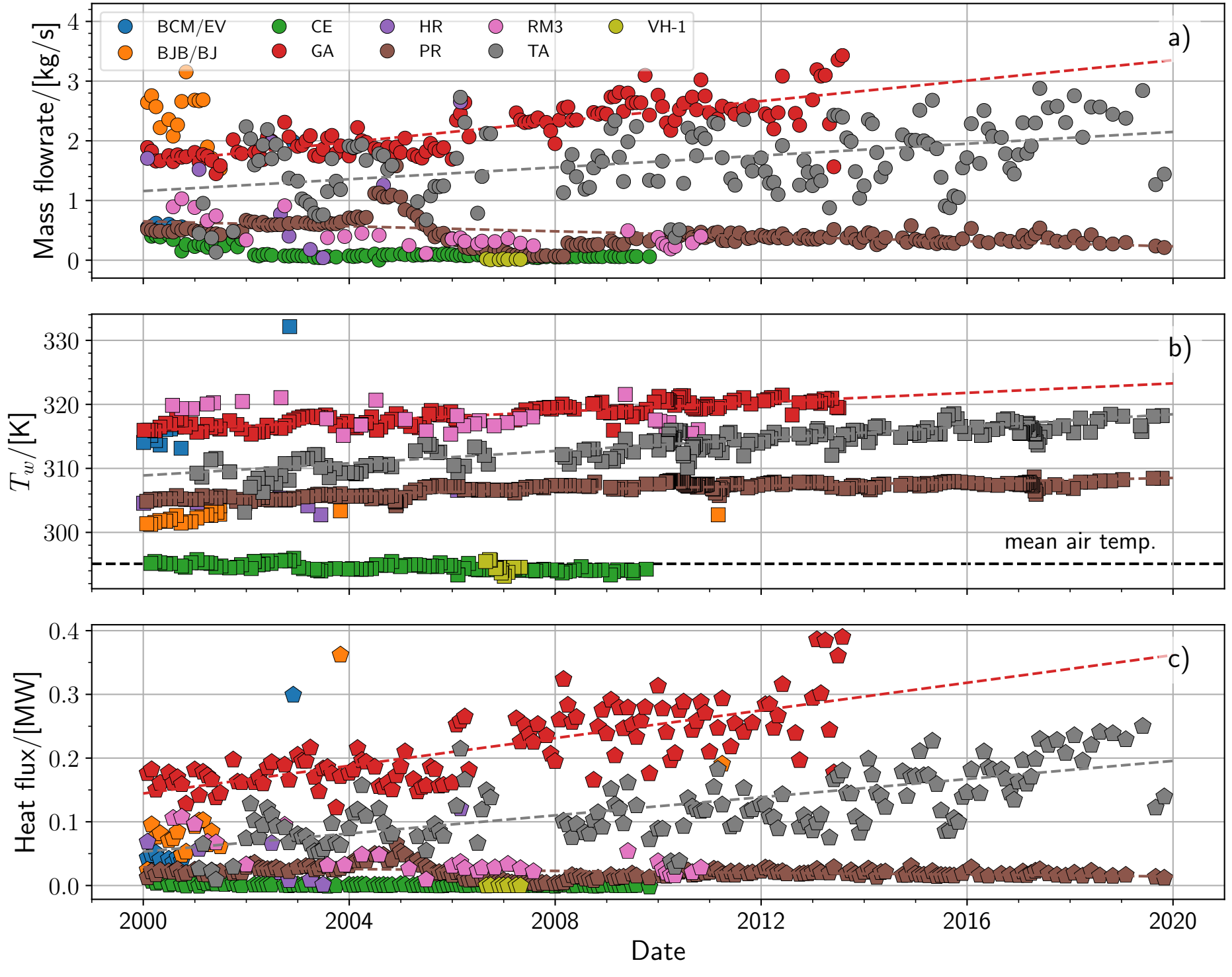
BCM/EV
BJB/BJ
CE
GA
HR
PR
RM3
TA
VH-1
a)
Mass flowrate/[kg/s]
b)
T_w/[K]
mean air temp.
c)
Heat flux/[MW]
Date
2000
2004
2008
2012
2016
2020

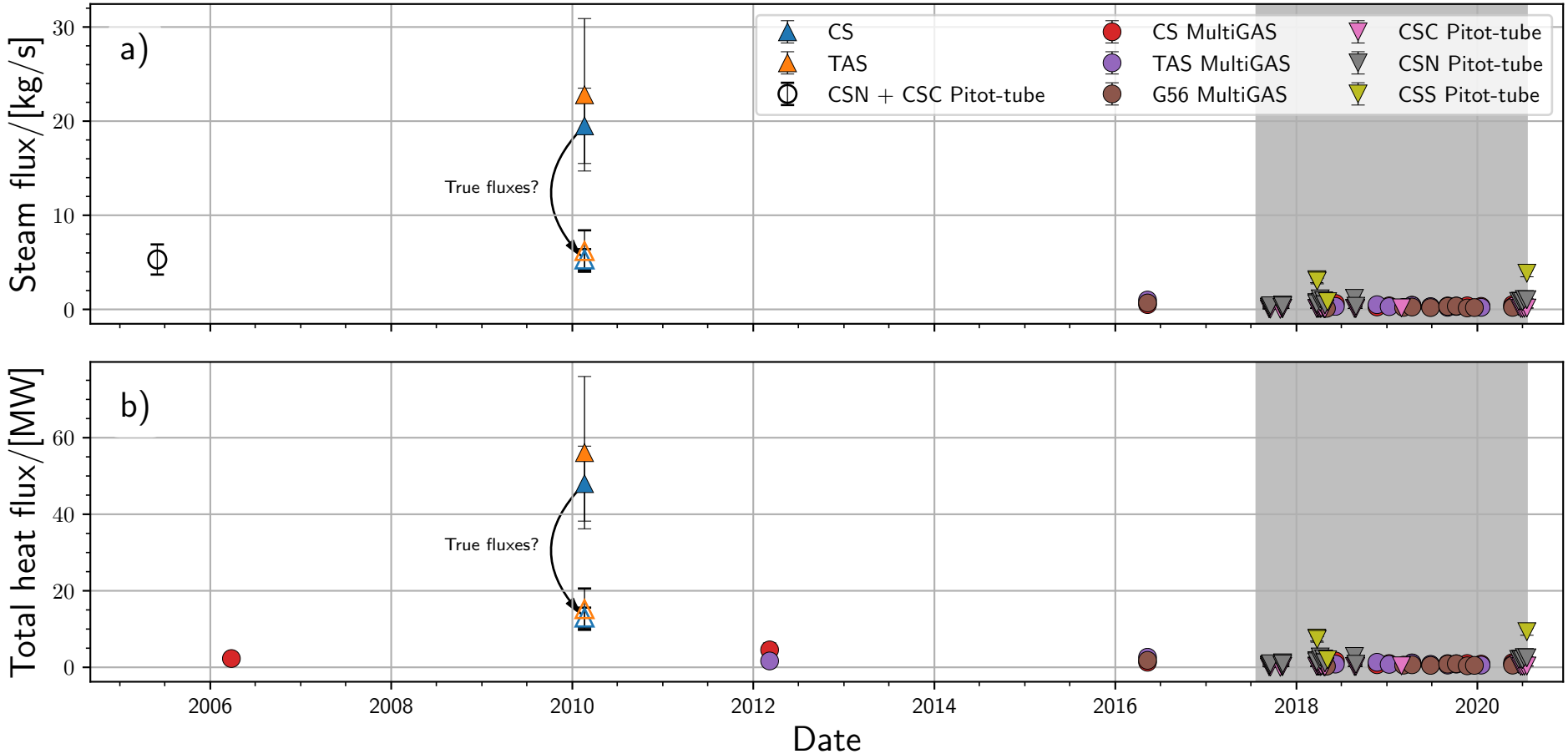
a)
b)
Steam flux/[kg/s]
Total heat flux/[MW]
True fluxes?
True fluxes?
CS
TAS
CSN + CSC Pitot-tube
CS MultiGAS
TAS MultiGAS
G56 MultiGAS
CSC Pitot-tube
CSN Pitot-tube
CSS Pitot-tube
0
10
20
30
0
20
40
60
2006
2008
2010
2012
2014
2016
2018
2020
Date

Grand Decouverte
(1467 m)

2004

TAS
NAPN
NAPE
G56
CSN
CSC
CSS
Breislack
1400 m
1300 m

Grand Decouverte
(1467 m)

2010

TAS
NAPN
NAPE
G56
CSN
CSC
CSS
Breislack
1400 m
1300 m

Grand Decouverte
(1467 m)

2013

TAS
NAPN
NAPE
G56
CSN
CSC
CSS
Breislack
1400 m
1300 m

Grand Decouverte
(1467 m)

2017

TAS
NAPN
NAPE
G56
CSN
CSC
CSS
Breislack
1400 m
1300 m

100 m

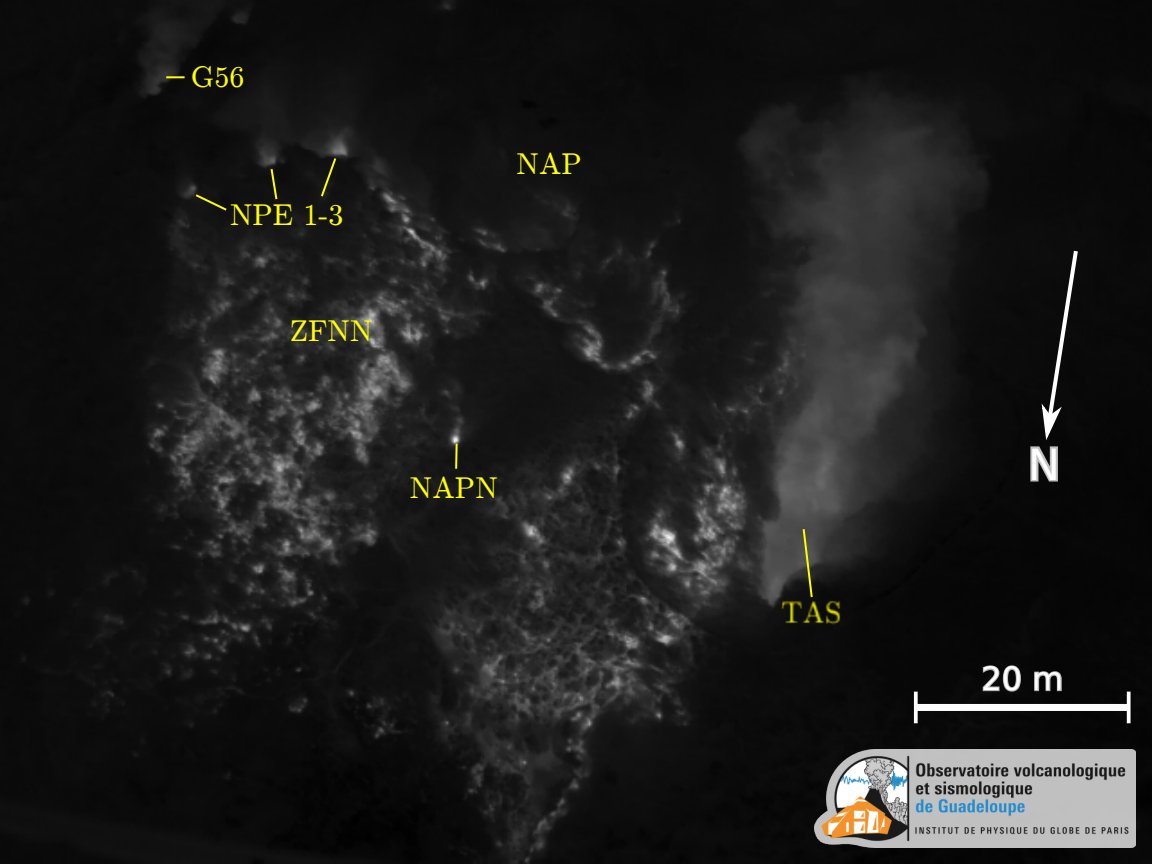
G56
NAP
NPE 1-3
ZFNN
NAPN
TAS
N
20 m
Observatoire volcanologique
et sismologique
de Guadeloupe
INSTITUT DE PHYSIQUE DU GLOBE DE PARIS

2004

2010

2013

2017

Route Cierne
FTY1 (North)
FTY1 (South)
FTY0
Matylis (upper)
Matylis (lower)
Ravine Claire
GAB
GA
1200 m
1100 m
100 m

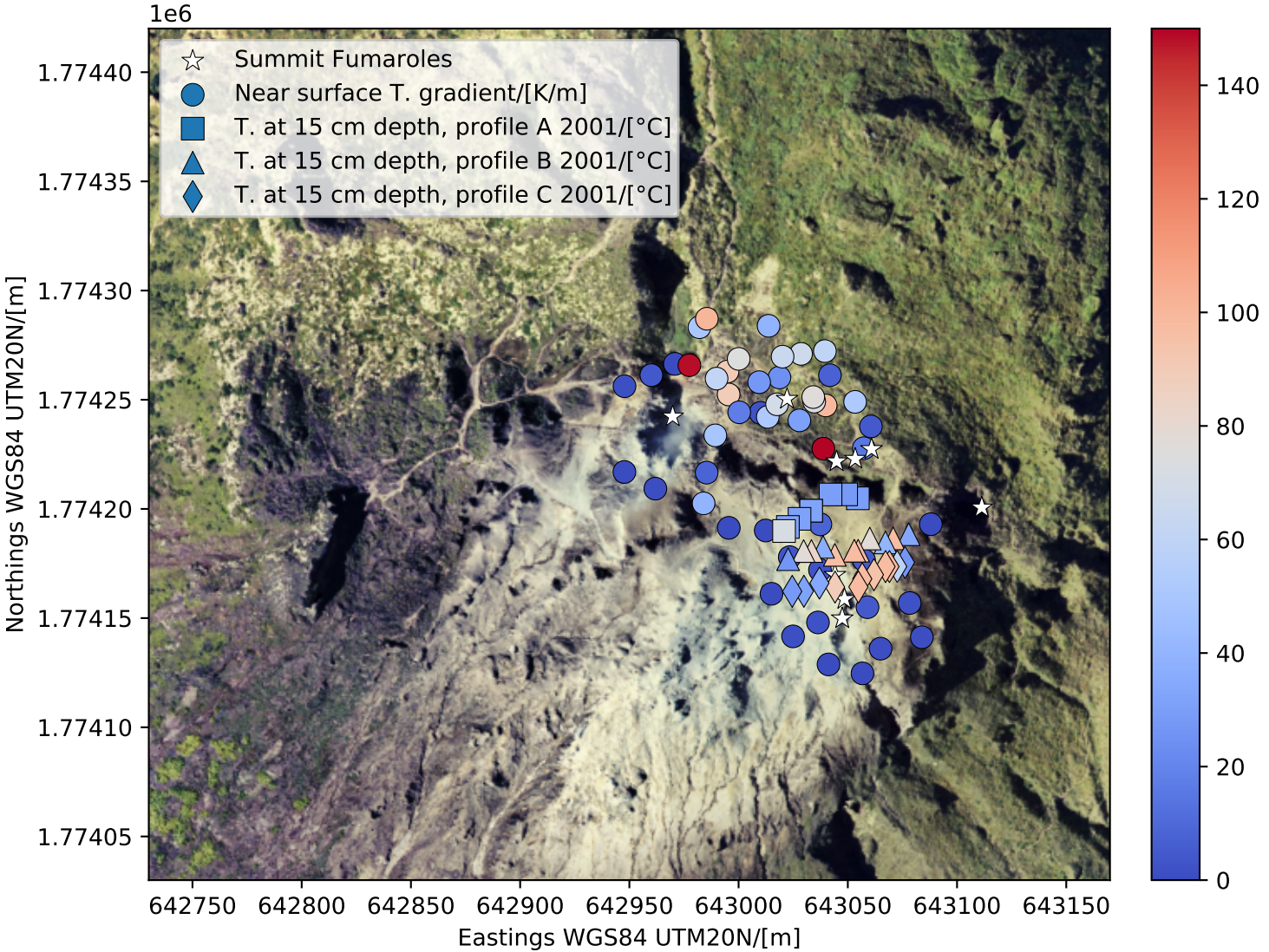
1e6
Summit Fumaroles
Near surface T. gradient/[K/m]
T. at 15 cm depth, profile A 2001/[°C]
T. at 15 cm depth, profile B 2001/[°C]
T. at 15 cm depth, profile C 2001/[°C]
1.77440
1.77435
1.77430
1.77425
1.77420
1.77415
1.77410
1.77405
Northings WGS84 UTM20N/[m]
642750
642800
642850
642900
642950
643000
643050
643100
643150
Eastings WGS84 UTM20N/[m]
140
120
100
80
60
40
20
0